JOURNAL OF PETROLOGY | VOLUME 48 | NUMBER 10 | PAGES 1875–1894 | 2007 | doi:10.1093/petrology/egm043

The Upper Crustal Evolution of a Large Silicic Magma Body: Evidence from Crystal-scale Rb–Sr Isotopic Heterogeneities in the Fish Canyon Magmatic System, Colorado

B. L. A. CHARLIER[1,2]*, O. BACHMANN[3,4], J. P. DAVIDSON[2], M. A. DUNGAN[3] AND D. J. MORGAN[5,6]

[1]DEPARTMENT OF EARTH SCIENCES, THE OPEN UNIVERSITY, WALTON HALL, MILTON KEYNES MK7 6AA, UK

[2]DEPARTMENT OF EARTH SCIENCES, UNIVERSITY OF DURHAM, SOUTH ROAD, DURHAM DH1 3LE, UK

[3]SECTION DES SCIENCES DE LA TERRE, UNIVERSITÉ DE GENÈVE, RUE DES MARAÎCHERS 13, CH-1205 GENEVA, SWITZERLAND

[4]DEPARTMENT OF EARTH AND SPACE SCIENCES, UNIVERSITY OF WASHINGTON, MAILSTOP 351310, SEATTLE, WA 98195-1310, USA

[5]LABORATOIRE GÉODYNAMIQUE DES CHAÎNES ALPINES, UMR5025, MAISON DES GÉOSCIENCES, 1381 RUE DE LA PISCINE, 38400 SAINT MARTIN D'HÈRES, FRANCE

[6]SCHOOL OF EARTH AND ENVIRONMENT, EARTH SCIENCE BUILDING, UNIVERSITY OF LEEDS, LEEDS LS2 9JT, UK

RECEIVED JANUARY 9, 2007; ACCEPTED JULY 12, 2007
ADVANCE ACCESS PUBLICATION AUGUST 20, 2007

Batholith-sized bodies of crystal-rich magmatic 'mush' are widely inferred to represent the hidden sources of many large-volume high-silica rhyolite eruptive units. Occasionally these mush bodies are ejected along with their trapped interstitial liquid, forming the distinctive crystal-rich ignimbrites known as 'monotonous intermediates'. These ignimbrites are notable for their combination of high crystal contents (35–55%), dacitic bulk compositions with interstitial high-silica rhyolitic glass, and general lack of compositional zonation. The 5000 km^3 Fish Canyon Tuff is an archetypal eruption deposit of this type, and is the largest known silicic eruption on Earth. Ejecta from the Fish Canyon magmatic system are notable for the limited compositional variation that they define on the basis of whole-rock chemistry, whereas ~45 vol. % crystals in a matrix of high-silica rhyolite glass together span a large range of mineral-scale isotopic variability (microns to millimetres). Rb/Sr isotopic analyses of single crystals (sanidine, plagioclase, biotite, hornblende, apatite, titanite) and sampling by micromilling of selected zones within glass plus sanidine and plagioclase crystals document widespread isotopic disequilibrium at many scales. High and variable $^{87}Sr/^{86}Sr_i$ values for euhedral biotite grains cannot be explained by any model involving closed-system radiogenic ingrowth, and they are difficult to rationalize unless much of this radiogenic Sr has been introduced at a late stage via assimilation of local Proterozoic crust. Hornblende is the only phase that approaches isotopic equilibrium with the surrounding melt, but the melt (glass) was isotopically heterogeneous at the millimetre scale, and was therefore apparently contaminated with radiogenic Sr shortly prior to eruption. The other mineral phases (plagioclase, sanidine, titanite, and apatite) have significantly lower $^{87}Sr/^{86}Sr_i$ values than whole-rock values (as much as −0·0005). Such isotopic disequilibrium implies that feldspars, titanite and apatite are antecrysts that crystallized from less radiogenic melt compositions at earlier stages of magma evolution, whereas highly radiogenic biotite xenocrysts and the development of isotopic heterogeneity in matrix melt glass appear to coincide with the final stage of the evolution of the Fish Canyon magma body in the upper crust. Integrated petrographic and geochemical evidence is consistent with pre-eruptive thermal rejuvenation of a near-solidus mineral assemblage from ~720 to 760°C (i.e. partial dissolution

*Corresponding author. Present address: Department of Earth Sciences, The Open University, Walton Hall, Milton Keynes MK7 6AA, UK. Telephone: +44(0)1908 652558. Fax: +44(0)1908 655151. E-mail: b.l.a.charlier@open.ac.uk

of feldspars + quartz while hornblende + titanite + biotite were crystallizing). Assimilation and blending of phenocrysts, antecrysts and xenocrysts reflects chamber-wide, low Reynolds number convection that occurred within the last ~10 000 years before eruption.

KEY WORDS: *Fish Canyon Tuff; Rb–Sr isotopes; microsampling; magmatic processes; crystal mush*

INTRODUCTION

In the varied spectrum of processes involved in continental silicic magmatism there is an important linkage between high-silica rhyolites and granites, with the former widely inferred to be generated as liquids expressed from underlying voluminous crystal mush that eventually forms granitoid plutons (e.g. Bachmann & Bergantz, 2004; Hildreth, 2004; Hildreth & Wilson, 2007, for reviews). Rhyolitic eruptives generally represent only a selected fraction of the liquids expressed, and these have usually undergone a subsequent prolonged history of further evolution that blurs the picture of their origins. Exposed granitic plutons have undergone long histories of near-solidus crystallization and subsolidus cooling that limit the amount of information obtainable about their generation (Davidson *et al.*, 2007). Occasionally, pyroclastic eruptions disgorge deep-seated 'crystal mushes' (i.e. magma bodies with crystal contents >30–40 vol. %) from the mid- to upper-crustal reservoirs that are inferred to lie below high-silica rhyolite magma chambers. Such pyroclastic units, which constitute the 'monotonous intermediate' group of ignimbrites [summarized by Hildreth (1981)], provide windows into processes within the mush zone that are otherwise obscured.

The largest examples of monotonous intermediate ignimbrites have been erupted in continental settings during magmatic 'flare-ups' (e.g. Francis *et al.*, 1989; de Silva, 1991; Lindsay *et al.*, 2001; Maughan *et al.*, 2002). These voluminous (500–5000 km^3 in volume) crystal-rich ignimbrites (35–50 vol. % crystals) commonly show little systematic variation in either elemental and isotopic compositions at the scale of whole-rock samples from first- to last-erupted magmas. Whole-rock and pumice compositions are typically dacitic (66–69 wt % SiO_2), but the interstitial glass is typically high-silica rhyolite (~76–77 wt % SiO_2) in composition. The magma bodies that fed the monotonous intermediate ignimbrites may represent an important reservoir for crystal-poor high-silica rhyolite magmas (Bachmann & Bergantz, 2004) that have, for whatever reason, undergone wholesale evacuation.

Multiple processes can be inferred to be occurring in crystal mush zones, all of which are ultimately fuelled by heat and mass transfer associated with mantle-derived mafic magmatism (Hildreth, 1981). Multi-stage modification of mantle-derived magmas may occur during ascent through the lithosphere via processes of fractional crystallization, magma mixing, contamination, assimilation of country rock and remobilization of earlier crystallized, largely or wholly solid material (e.g. Pitcher *et al.*, 1985; Hildreth & Moorbath, 1988; Johnson *et al.*, 1989; DePaolo *et al.*, 1992; Pitcher, 1993). Such processes inevitably result in some degree of textural and/or isotopic disequlibrium, which subsequently may be partly homogenized during extraction of interstitial high-silica rhyolite melt, or slow solidification of the mush to form a pluton. Petrological studies of intermediate volcanic rocks (and related mineral-specific compositional relations) have often identified crystal–melt disequilibrium, implying that some phases did not grow from their host melts (e.g. Tsuchiyama, 1985; Dungan *et al.*, 2001; Dungan & Davidson, 2004). Isotopic compositions determined by microsampling among and within diverse crystal components of magmatic rocks have been used to evaluate magmatic processes, as they permit 'fingerprinting' of multiple implicated components (e.g. Geist *et al.*, 1988; Simonetti & Bell, 1993; Davidson & Tepley, 1997; Davidson *et al.*, 2005a). Zonations in isotopic composition documented by core-to-rim traverses across single crystals, especially when these traverses are tied to major element zoning profiles and textural features such as resorption surfaces, provide a high-resolution temporal record of the isotopic evolution of a magma during the growth of the relevant crystal phases (e.g. Hora, 2003).

A high degree of mineral and melt isotopic disequilibrium is preserved down to the scale of individual crystals in the Fish Canyon magma (~68% SiO_2). This rapidly erupted and quenched, batholithic-scale crystal mush is the archetypical monotonous-intermediate ignimbrite and the most voluminous known example of this phenomenon. The Rb–Sr system is applied here to whole-rock samples, single crystals and microgram-sized mineral microsampled aliquots to illuminate petrological processes occurring in a batholith-scale crystal mush prior to eruption. A combination of sampling from thick sections by micromilling coupled with new refinements in analytical techniques (Charlier *et al.*, 2006) allow Sr isotopic differences to be measured on a sub-millimetre scale to an external precision of 50 ppm. These data have been combined with diffusion modelling of trace-element profiles to document not only the isotopic diversity within a thin-section sized domain but also to estimate the timescale for assimilation events in the crystal mush that was parental to the Fish Canyon Tuff and co-magmatic units.

THE FISH CANYON TUFF

The ~5000 km^3 Fish Canyon Tuff (FCT), is the product of the largest known pyroclastic eruption on Earth. It was erupted at ~28 Ma from the La Garita caldera (Fig. 1), and

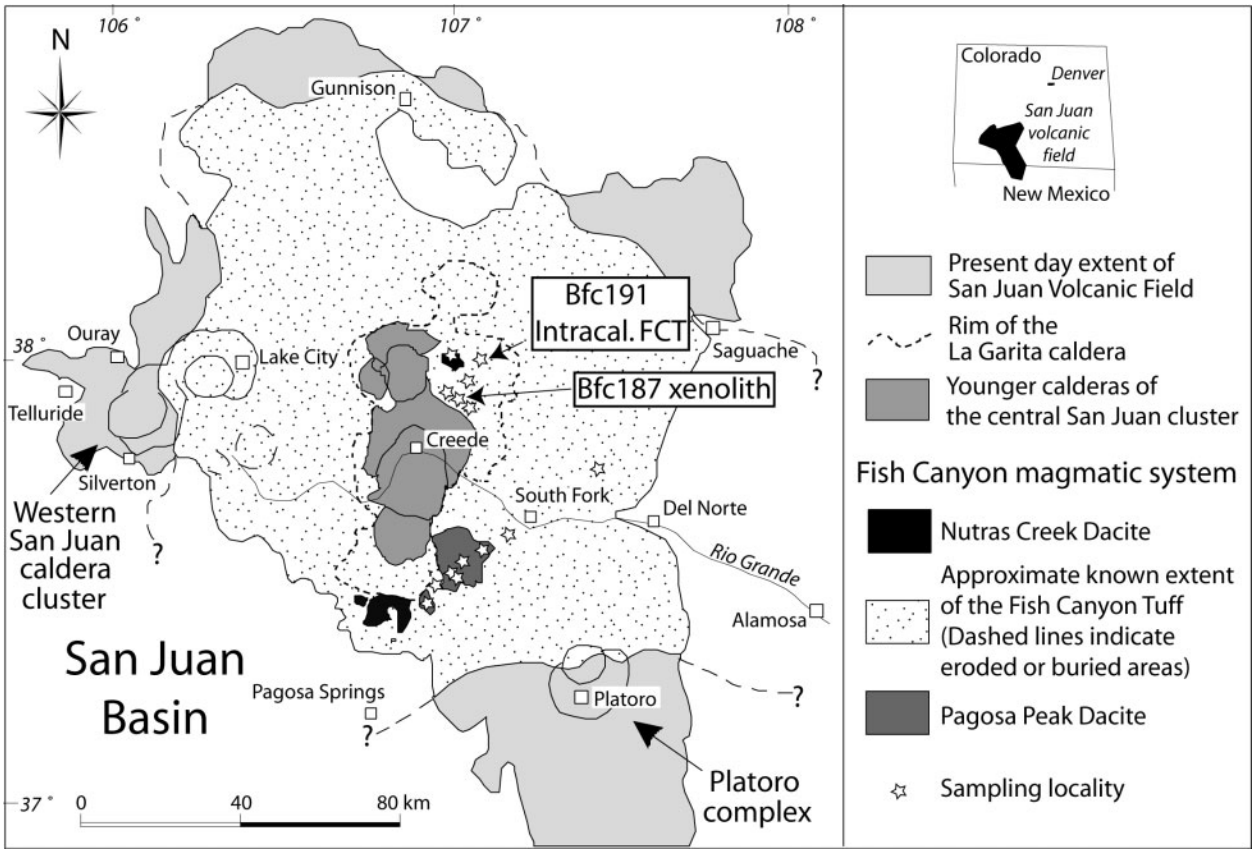

Fig. 1. Location map of the San Juan volcanic field, showing the distribution of the three units of the Fish Canyon magmatic system and the sampling localities (modified from Bachmann *et al.*, 2007). The localities of the two samples used for micromilling (BFCl187 holocrystalline xenolith and BFCl91 intracaldera Fish Canyon Tuff) are marked.

is the second of eight major Oligocene ignimbrites with sources in the central San Juan caldera cluster in Colorado (Lipman, 2000). The FCT is characterized by a uniform mineral assemblage, few systematic geochemical variations from early to late-erupted material, and a lack of evidence for compositional and/or thermal gradients in the parental magma body (Steven & Lipman, 1976; Whitney & Stormer, 1985; Lipman, 2000; Bachmann *et al.*, 2002). The same magma that fed the FCT was also tapped by an earlier low-energy pyroclastic eruption (Pagosa Peak Dacite) and by a later lava flow (the Nutras Creek Dacite: Lipman *et al.*, 1997; Bachmann *et al.*, 2000). These three compositionally identical products of what we refer to as the Fish Canyon magmatic system contrast with the diverse compositions and mineral assemblages of other large ignimbrites that were erupted from the central San Juan caldera cluster (Riciputi *et al.*, 1995; Lipman, 2000). Fish Canyon juvenile material is dacitic (68 ± 1 wt % SiO_2) and crystal-rich (~45 vol. % crystals), and it contains a near-solidus mineral assemblage comprising plagioclase, K-feldspar, quartz, hornblende, biotite, titanite, Fe–Ti oxides, apatite, zircon, and (rare) pyrrhotite (in order of decreasing abundance). Interstitial glasses in Fish Canyon magma samples are microlite-free, high-silica rhyolite (76·5–78 wt % SiO_2, calculated volatile-free; Bachmann *et al.*, 2005).

Studies of the mineralogy and petrology of the FCT (e.g. Whitney & Stormer, 1985; Bachmann *et al.*, 2002) have shown that, despite large-scale homogeneity in whole-rock magma composition, there is abundant textural and compositional complexity at the crystal scale and that these complexities can be used to constrain the operation of magmatic processes. Quartz, sanidine and 30–50 vol. % of the plagioclase occur as resorbed, amoeboid grains. In contrast, hornblende (0·5–3 mm long) and biotite (0·5–5 mm across) are euhedral crystals with no physical evidence for reaction with host melt. Interstitial glass, representing the melt composition at the time of eruption, is preserved in multiple samples of the Pagosa Peak Dacite and FCT as brown pools within clasts, as well as individual shards up to a few millimetres long. These high-SiO_2 rhyolite glasses have unusually high contents of Ba (480–560 ppm: Bachmann *et al.*, 2002, 2005) and Sr (93–131 ppm: Bachmann *et al.*, 2005, and this study) for such otherwise-evolved compositions, consistent with the textural evidence that the feldspars were undergoing

resorption prior to eruption. An isobaric, ~45°C temperature increase from ~715°C to 760°C during the late evolution of the FCT magma is inferred from Al-zoning profiles in hornblendes (Bachmann & Dungan, 2002). 'Gas sparging' (upward percolation of a hot H_2O-rich fluid phase, released from an underplated, less-evolved magma, through the largely solidified FCT crystal mush) has been proposed as a potential mechanism to induce the observed thermal rejuvenation of the magma (Bachmann & Bergantz, 2003, 2006).

ANALYTICAL METHODS AND SAMPLES

We only summarize here the techniques used in this study, and the reader is referred to Charlier *et al.* (2006) for fuller details. Microsampling for Rb/Sr isotopic determinations was performed on 100–120 μm polished thick sections, using a New Wave® Micromill to generate either a powder slurry from a target area within a single crystal, or to excise a single whole grain from within thick sections. The amount of sample produced by milling (10–100 μg) is primarily dependent on the depth of penetration of the mill bit (and thus the section thickness), and the number of points sampled (see Charlier *et al.*, 2006, fig. 2). Because Sr concentrations in plagioclase, sanidine and glass were all sufficiently high (>900, >400 and >90 ppm, respectively) these materials were sampled directly using the micromill to produce a slurry. For phases with lower Sr concentrations (e.g. hornblende and biotite; >32 and >6 ppm), single crystals were excised from thick sections by milling around the crystal of interest, then using a dentistry pick to carefully prise the crystal from the section. For analyses of titanite and apatite, single crystals were picked by hand from roughly crushed and sieved material. Single crystal analyses of plagioclase and sanidine were also carried out to compare the $^{87}Sr/^{86}Sr$ variations found at the intra-grain level with those found at the inter-grain level.

Slurry samples from micromilling were collected with a micropipette, dried and weighed to ±0·1 μg. Excised and picked individual crystals were cleaned first in methanol followed by water, dried and then weighed. After addition of the requisite amount of a high-purity ^{84}Sr–^{87}Rb spike, the samples were dissolved in 3·5 ml Savillex capsules using concentrated $HF + HNO_3$ and finally equilibrated with 2·5M HCl. Quartz glass microcolumns filled with ~0·75 ml of Dowex AG 50W-X8 cation exchange resin were used for initial separation of Rb and Sr. The Sr eluate was collected and further purified using a 50 μl column filled with Sr-Spec® resin.

A Ta emitter solution, which enhances Sr ionization efficiency, was used to load nanogram quantities of Sr onto single outgassed Re filaments for thermal ionization mass spectrometry (TIMS) analysis. All Sr aliquots were analysed using a Finnigan Triton TIMS instrument in static collection mode with simultaneous monitoring of ^{85}Rb. The isotopic composition of Rb remaining in the Sr eluate was monitored prior to Sr ionization (to check for a possible spike contribution). Sr mass fractionation corrections used $^{88}Sr/^{86}Sr = 8{\cdot}375211$ and an exponential law relationship. Rb was run on a Neptune multicollector inductively coupled plasma mass spectrometer using admixed Zr to correct for instrumental bias. No blank corrections were applied because total procedure blanks were ~3–10 pg for Sr and ~10–25 pg for Rb, which are negligible compared with the sample loads of 1–10 ng for both elements. Long-term external reproducibility of Sr measurements of the NBS987 standard during the course of this study and of a similar load size to micromilled samples (~3 ng Sr) was $^{87}Sr/^{86}Sr = 0{\cdot}710258 \pm 36$ 2SD (50 ppm) and $^{84}Sr/^{86}Sr = 0{\cdot}056489 \pm 24$ 2SD (433 ppm), where $n = 288$. The uncertainty of the $^{87}Rb/^{86}Sr$ ratio is ~0·25% using the measurement techniques detailed by Charlier *et al.* (2006).

Samples of Fish Canyon Tuff were chosen from the sample suite collected for the doctoral thesis work of Bachmann (2001), and the sampling locations are shown in Fig. 1. The selected samples showed little or no evidence of alteration or hydration. The microsampling and single crystal work was carried out on thick sections cut from two samples.

(1) As all samples of Fish Canyon magma are very similar, we chose a large welded pumice fragment from the intra-caldera facies of the Fish Canyon Tuff (Sample BFC191) because it contains all the relevant mineral phases in addition to particularly fresh interstitial glass in areas large enough to sample, and because this large juvenile clast (fiamme) warrants against non-magmatic contamination. Feldspars from two other sections of this sample were analysed to ensure that the full range of feldspar compositions had been covered.

(2) Sample BFC187 (co-magmatic holocrystalline xenolith from the same location as BFC191, with a TIMS U–Pb age from zircon indistinguishable from those of Fish Canyon Tuff zircons: Bachmann *et al.*, 2007) was chosen for its coarse grain size and the probability that it crystallized at the margins of the magma chamber.

In addition to these samples, we analysed 24 whole-rock powders spanning the lithological diversity, eruptive order, and geographical range of the Fish Canyon Tuff and its precursor, the Pagosa Peak Dacite (Bachmann, 2001). Included in this whole-rock suite are two samples of coarse-grained co-magmatic xenoliths (CSGR14 and CSGR16) and two lithic fragments of amphibolitic

basement (MLX Amph2 and Amph3) from the northern intra-caldera FCT.

Prior to microsampling, electron microprobe traverses across selected feldspar crystals were carried out using a Cameca SX50 at the University of Lausanne. Standard analytical conditions were used (voltage 15 kV, filament current 15 nA, beam diameter 1–2 μm), and care was taken to avoid Na loss by using a shorter counting time on Na. Only analyses with totals in the range 99–101 % were accepted.

RESULTS

Sr isotopic data plus Rb and Sr concentrations are presented for whole-rock powders, single crystals and micromilled aliquots in Table 1. Figures 2a–e show the whole-rock and single crystal data on plots of $^{87}Sr/^{86}Sr$ initial ratios ($^{87}Sr/^{86}Sr_i$) vs $^{87}Rb/^{86}Sr$, wherein the axes are variably scaled to the appropriate range of values. The calculated values of $^{87}Sr/^{86}Sr_i$ are a function of the age (28·02 Ma on the basis of $^{40}Ar/^{39}Ar$ ages on sanidine; Renne *et al.*, 1998), the Rb/Sr ratio of the sample, and the overall 2σ uncertainty associated with these values. The last variable quadratically combines the 2σ external standard reproducibility of the $^{87}Sr/^{86}Sr$ measurement, the within-run measurement uncertainties, the uncertainty on the age used for correction ($28{\cdot}02 \pm 0{\cdot}28$ Ma: Renne *et al.*, 1998), and the uncertainty on the $^{87}Rb/^{86}Sr$ ratio.

Whole-rock Rb–Sr data

The majority of the FCT and Pagosa Peak Dacite whole-rock samples define ranges in $^{87}Sr/^{86}Sr_i$ from 0·70626 to 0·70657 and $^{87}Rb/^{86}Sr$ from 0·49 to 0·93 (Fig. 2b). We stress that these ranges are restricted in comparison with the entire dataset. The two less radiogenic, low $^{87}Rb/^{86}Sr$ data points that plot to the left of the main group are: (1) a whole-rock sample of distal tuff (BFCElep), which is inferred to have lost some ash through winnowing during transport (Whitney & Stormer, 1985; Bachmann *et al.*, 2002); (2) an andesitic enclave from the FCT intracaldera facies (BFC138). Its low $^{87}Sr/^{86}Sr_i$ value is consistent with its less evolved composition. The two most radiogenic whole-rock values from the Fish Canyon system are from co-magmatic xenoliths [CSGR14 (Fig. 2b) and BFC187 (Fig. 2c)], both of which have been dated by U–Pb single-grain zircon TIMS analyses (Bachmann *et al.*, 2007) at ~28·0–28·6 Ma (i.e. indistinguishable from zircon ages of the main FCT deposit). BFC187 is atypical in that it has by far the most radiogenic $^{87}Sr/^{86}Sr_i$ value (0·70759), but not an especially elevated value of $^{87}Rb/^{86}Sr$ (0·70). MLX Amph2 and MLX Amph3 are accidental lithic fragments (not magmatic xenoliths) of the surrounding amphibolitic Precambrian basement within which the San Juan Tertiary magmas evolved (Riciputi *et al.*, 1995; Smith *et al.*, 1999; Wobus *et al.*, 2001). They were sampled in the northern intracaldera FCT facies (same general area as BFC187 and BFC191) and have extremely radiogenic $^{87}Sr/^{86}Sr_i$ values (0·94235 and 0·79182), not plotted for the sake of scale.

Single mineral Rb–Sr data

Values of $^{87}Sr/^{86}Sr_i$ and $^{87}Rb/^{86}Sr$ determined on single grains of FCT apatite, titanite, hornblende, biotite, sanidine and plagioclase span very large ranges (0·70578–0·72942 and 0·002–172·5, respectively). The lowest $^{87}Rb/^{86}Sr$ values (<0·02) are from apatite and plagioclase (Fig. 2a), whereas the highest are from biotites (8·01–172·5: Fig. 2d and e). Large euhedral single apatites (~200–300 μm in length) with Sr concentrations of 436–685 ppm, and 0·3–1·4 ppm Rb, define a restricted range in $^{87}Sr/^{86}Sr_i$ of 0·70623–0·70634 and are generally less radiogenic than plagioclase, which defines a larger range from 0·70632 to 0·70670. Single euhedral titanite crystals (~200 μm) also have variable $^{87}Sr/^{86}Sr_i$ (0·70578–0·70644), and four of these yield the least radiogenic values recorded in this study. As Rb concentrations in titanite are similar to those in apatite (0·5–1·3 ppm), the higher $^{87}Rb/^{86}Sr$ values for titanite (0·04–0·12) reflect much lower Sr concentrations (30·5–52·9 ppm).

Single euhedral hornblende crystals extracted from glassy fiamme (Fig. 2b) define a restricted range in $^{87}Rb/^{86}Sr$ and $^{87}Sr/^{86}Sr$ (0·15–0·22 and 0·70656–0·70667), but have values that are distinct from, and more radiogenic than, both titanite and apatite. They are, however, within the range of $^{87}Sr/^{86}Sr_i$ values, albeit towards the more radiogenic end of the plagioclase and whole-rock analyses.

Fish Canyon sanidine crystals are invariably resorbed and they occur as large amoeboid grains that resemble comparably resorbed quartz grains. The sanidines often contain small inclusions of plagioclase, although hornblende, biotite, oxides, apatite and titanite are occasionally present in minor quantities. These textural similarities render picking of single 'clean' sanidine grains very difficult, and it is probable that some of the grains contained minor mineral and/or glass inclusions. Such complexities may be the cause of variable Sr and Rb concentrations in the sanidine single-crystal population (576–933 ppm and 74–149 ppm, respectively), which may have led in turn to large ranges for $^{87}Rb/^{86}Sr$ (0·30–0·73). Values of $^{87}Sr/^{86}Sr_i$ in sanidine (0·70632–0·70672), not surprisingly, encompass the ranges defined by plagioclase, hornblende, titanite and apatite data, with the exception of the four least radiogenic titanite analyses.

Glass analyses were performed by micromilling areas of crystal-free fresh brown glass directly from a single thick section (BFC191; Fig. 3). These aliquots are sufficiently large to yield 10–20 ng Sr for isotopic analysis (Fig. 2c). Concentrations of Rb and Sr are both high (161–180 ppm and 93–131 ppm respectively), but with a greater range seen in the Sr concentration data. $^{87}Rb/^{86}Sr$ varies from 3·1 to 5·4

Table 1: Rb and Sr concentration data, and Sr isotopic data for samples from the Fish Canyon Tuff

Sample ID	Sr (ppm)	Rb (ppm)	$^{87}Rb/^{86}Sr$	$^{87}Sr/^{86}Sr_M$*	$^{87}Sr/^{86}Sr_i$†
Whole-rocks					
BFC12	461·1	125·6	0·788	0·706843 ± 12	0·706529 ± 45
BFC37	428·9	120·1	0·81	0·706720 ± 12	0·706398 ± 45
BFC83	439·2	119·8	0·789	0·706704 ± 10	0·706390 ± 41
BFC97	466·5	117·5	0·729	0·706707 ± 12	0·706417 ± 45
BFC98	496·5	110·5	0·644	0·706638 ± 10	0·706382 ± 41
BFC99	429	121·7	0·821	0·706704 ± 10	0·706377 ± 41
BFC100	448	119·7	0·773	0·706704 ± 6	0·706396 ± 34
BFC101	427·1	120·7	0·817	0·706731 ± 6	0·706406 ± 34
BFC102	438·7	120·6	0·795	0·706759 ± 6	0·706443 ± 32
BFC149	440·3	124·3	0·817	0·706714 ± 10	0·706389 ± 41
MD96-7	443·1	122·8	0·802	0·706686 ± 8	0·706367 ± 38
BFC84	503·5	133·8	0·769	0·706642 ± 14	0·706336 ± 50
BFC113	465·3	117·2	0·729	0·706614 ± 12	0·706324 ± 45
BFC124	486·9	109·6	0·651	0·706657 ± 12	0·706398 ± 45
BFC125	463	116·1	0·725	0·706637 ± 12	0·706348 ± 45
BFC129	455·5	117·2	0·744	0·706745 ± 12	0·706449 ± 38
BFCELEP	570·3	96	0·487	0·706546 ± 6	0·706352 ± 34
BFC115	436·4	122·8	0·814	0·706689 ± 8	0·706365 ± 38
BFC138	541·9	100·6	0·537	0·706476 ± 8	0·706262 ± 38
CSGR 14	477	90·8	0·551	0·706793 ± 10	0·706574 ± 41
CSGR 16	384	123·4	0·93	0·706785 ± 14	0·706415 ± 50
MLX Amph 2	91	129	14·964	0·948302 ± 12	0·942347 ± 33
MLX Amph 3	459·9	253·3	5·728	0·794095 ± 20	0·791815 ± 39
BFC187	387	93·4	0·698	0·707874 ± 16	0·707592 ± 38
Single grains					
Apatite					
Apa-1	509·7	0·5	0·003	0·706288 ± 13	0·706283 ± 25
Apa-2	514	0·8	0·004	0·706347 ± 9	0·706342 ± 23
Apa-3	524·5	1·2	0·006	0·706284 ± 15	0·706278 ± 26
Apa-4	435·8	0·3	0·002	0·706288 ± 10	0·706283 ± 23
Apa-5	565·7	1·4	0·007	0·706283 ± 15	0·706277 ± 26
Apa-6	685·1	1·1	0·005	0·706234 ± 8	0·706229 ± 23
Titanite					
Sph-1	40·1	0·6	0·039	0·706318 ± 10	0·706088 ± 23
Sph-2	30·5	1·3	0·12	0·706121 ± 30	0·705782 ± 37
Sph-3	42·2	1	0·066	0·706609 ± 23	0·706380 ± 31
Sph-4	32·4	0·6	0·051	0·706377 ± 16	0·706087 ± 27
Sph-5	41·9	0·8	0·055	0·706303 ± 17	0·706076 ± 27
Sph-6	52·9	0·5	0·026	0·706619 ± 18	0·706443 ± 28
Hornblende					
Hbl-1	32	2·3	0·203	0·706737 ± 26	0·706639 ± 34
Hbl-2	37·4	2·4	0·184	0·706734 ± 24	0·706648 ± 32
Hbl-3	43·6	3·3	0·215	0·706650 ± 18	0·706556 ± 28
Hbl-5	48·3	3·5	0·209	0·706671 ± 25	0·706579 ± 33
Hbl-6	51·2	2·7	0·152	0·706743 ± 26	0·706672 ± 34

(continued)

Table 1: Continued

Sample ID	Sr (ppm)	Rb (ppm)	$^{87}Rb/^{86}Sr$	$^{87}Sr/^{86}Sr_M$*	$^{87}Sr/^{86}Sr_i$†
Biotite					
191Bi-1	19	344·8	50·034	0·727008 ± 47	0·707022 ± 206
191Bi-2	30·5	321·5	28·856	0·719230 ± 30	0·707709 ± 121
191Bi-3	24·3	339·7	37·61	0·722837 ± 27	0·707837 ± 154
191Bi-4	39	316	24·475	0·716466 ± 29	0·706691 ± 104
191Bi-5	15·7	360·6	63·891	0·732626 ± 37	0·707079 ± 258
191Bi-6	17·3	320·9	49·951	0·728222 ± 28	0·708298 ± 202
191Bi-7	43·7	329·1	20·411	0·715108 ± 21	0·706965 ± 87
191Bi-8	18·5	336·9	49·281	0·726890 ± 39	0·707229 ± 201
191Bi-9	23·6	328·2	37·73	0·723391 ± 39	0·708338 ± 157
191Bi-10	64·2	293·7	13·026	0·712471 ± 12	0·707282 ± 57
191Bi-11	87·2	263·9	8·611	0·711124 ± 12	0·707693 ± 42
191Bi-12	38·4	300·3	22·276	0·716559 ± 8	0·707685 ± 92
191Bi-13	98·9	279·8	8·05	0·711317 ± 17	0·708109 ± 42
191Bi-14	59·4	290·7	13·932	0·712824 ± 10	0·707274 ± 60
191Bi-15	46·7	296·1	18·056	0·714383 ± 15	0·707190 ± 76
191Bi-16	61	282·1	13·164	0·712729 ± 13	0·707482 ± 58
187Bi-1	16·2	270·6	47·103	0·741917 ± 30	0·723144 ± 59
187Bi-2	8·6	364·2	117·874	0·761039 ± 156	0·714078 ± 193
187Bi-3	26·6	342·6	35·836	0·724797 ± 21	0·710521 ± 59
187Bi-4	6·7	411·4	169·855	0·780332 ± 94	0·712675 ± 326
187Bi-5	8·7	244·9	79·213	0·760988 ± 52	0·729416 ± 98
187Bi-6	5·8	356·8	172·544	0·785299 ± 85	0·716557 ± 282
Sanidine					
SG San-1	589·8	149·2	0·732	0·706659 ± 25	0·706368 ± 47
SG San-2	714·3	74·1	0·3	0·706732 ± 28	0·706612 ± 49
SG San-3	891·9	121·7	0·395	0·706497 ± 54	0·706340 ± 82
SG San-4	933·1	145·3	0·377	0·706478 ± 8	0·706317 ± 37
SG San-5	572·7	122·9	0·621	0·706767 ± 4	0·706520 ± 30
SG San-6	683·5	111·8	0·473	0·706656 ± 4	0·706468 ± 31
SG San-7	446·1	112·3	0·728	0·707014 ± 6	0·706724 ± 31
SG San-8	618·1	115·2	0·539	0·706732 ± 5	0·706517 ± 31
SG San-9	869·1	111·9	0·373	0·706538 ± 5	0·706389 ± 31
SG San-10	593	96·6	0·471	0·706741 ± 11	0·706554 ± 34
SG San-11	731·4	84·4	0·334	0·706571 ± 15	0·706439 ± 37
SG San-12	813·5	85·6	0·304	0·706592 ± 4	0·706471 ± 31
SG San-13	576	89·6	0·45	0·706636 ± 9	0·706457 ± 33
SG San-14	861·5	100·2	0·337	0·706556 ± 6	0·706422 ± 31
Plagioclase					
SG Plg-1	1062·6	2·3	0·006	0·706372 ± 11	0·706369 ± 34
SG Plg-2	980·6	1·9	0·006	0·706352 ± 4	0·706350 ± 30
SG Plg-3	1014·8	1·6	0·005	0·706507 ± 6	0·706505 ± 31
SG Plg-4	1008·7	1·7	0·005	0·706702 ± 14	0·706700 ± 36
SG Plg-5	1055·2	1·2	0·003	0·706439 ± 6	0·706438 ± 31
SG Plg-6	1287·9	1·5	0·003	0·706419 ± 10	0·706404 ± 23

(continued)

Table 1: Continued

Sample ID	Sr (ppm)	Rb (ppm)	$^{87}Rb/^{86}Sr$	$^{87}Sr/^{86}Sr_{M}$*	$^{87}Sr/^{86}Sr_{i}$†
SG Plg-7	1317	4·4	0·009	0·706341 ± 8	0·706324 ± 23
SG Plg-8	1124·7	1·9	0·005	0·706340 ± 5	0·706322 ± 22
SG Plg-9	977·3	1·3	0·004	0·706574 ± 12	0·706572 ± 34
SG Plg-10	931·5	1·9	0·006	0·706707 ± 15	0·706705 ± 37
SG Plg-11	940·8	2	0·006	0·706377 ± 2	0·706375 ± 30
SG Plg-12	983·2	1·7	0·005	0·706381 ± 3	0·706379 ± 30
SG Plg-13	1013·3	4	0·011	0·706501 ± 6	0·706496 ± 31
SG Plg-14	979·2	1·3	0·004	0·706551 ± 13	0·706549 ± 35
Micromilled samples					
Glass					
Gls-1	104·5	172·3	3·348	0·708458 ± 44	0·707075 ± 57
Gls-2	108·1	167·2	3·871	0·708499 ± 22	0·706818 ± 54
Gls-3	131·1	172·1	3·102	0·708608 ± 67	0·707294 ± 86
Gls-4	121	154·4	3·095	0·708550 ± 33	0·707227 ± 41
Gls-5	95·2	180·3	5·431	0·708641 ± 35	0·706459 ± 51
Gls-6	102	174·1	4·894	0·708467 ± 21	0·706502 ± 40
Gls-7	93·3	161·8	4·971	0·708463 ± 34	0·706465 ± 48
Sanidine					
San1-plagincl	1010·7	6·9	0·019	0·706403 ± 6	0·706379 ± 22
San1-2	660·5	80·2	0·321	0·706729 ± 19	0·706582 ± 31
San1-3	633·2	99·8	0·397	0·706715 ± 14	0·706542 ± 34
San1-4	727·1	121·8	0·421	0·706728 ± 23	0·706545 ± 40
San1-5	683·3	120·0	0·439	0·706859 ± 17	0·706669 ± 39
San1-6	697·1	116·5	0·422	0·706887 ± 18	0·706702 ± 37
San2-1	866·1	118·7	0·351	0·706600 ± 29	0·7064445 ± 40
San2-2	806·7	117·8	0·366	0·706612 ± 22	0·706452 ± 38
San2-3	796·3	120·7	0·381	0·706596 ± 30	0·706430 ± 43
San2-4	979·9	130·4	0·325	0·706597 ± 30	0·706457 ± 44
San2-5	867·8	118·1	0·340	0·706586 ± 27	0·706439 ± 40
San2-6	632·0	118·8	0·465	0·706693 ± 35	0·706492 ± 52
Plagioclase					
Plg1-1	1011·5	10·3	0·029	0·706402 ± 12	0·706371 ± 24
Plg1-2	919·7	6·2	0·019	0·706386 ± 8	0·706358 ± 23
Plg1-3	1008·6	15·8	0·044	0·706276 ± 9	0·706242 ± 23
Plg1-4	1054·4	29·6	0·078	0·706252 ± 8	0·706204 ± 23
Plg2-1	1200·4	8·1	0·019	0·706367 ± 13	0·706345 ± 25
Plg2-2	885·6	8·2	0·026	0·706587 ± 8	0·706558 ± 23
Plg2-3	1133·4	4·8	0·012	0·706348 ± 15	0·706328 ± 26
Plg3-4	906·9	6·1	0·019	0·706388 ± 8	0·706362 ± 23
Plg3-5	871·9	7·9	0·026	0·706486 ± 8	0·706455 ± 23
Plg3-6	1201·9	8·1	0·019	0·706350 ± 9	0·706329 ± 23

All analyses were carried out at the Arthur Holmes Isotope Geology Laboratory at the University of Durham.
*Measured $^{87}Sr/^{86}Sr$ ratios, where the uncertainties refer to the least significant digits and are 2σ mean within-run precisions.
†Age-corrected $^{87}Sr/^{86}Sr$ ratios, where the uncertainties refer to the least significant digits and are 2σ total external precisions (see text for details).

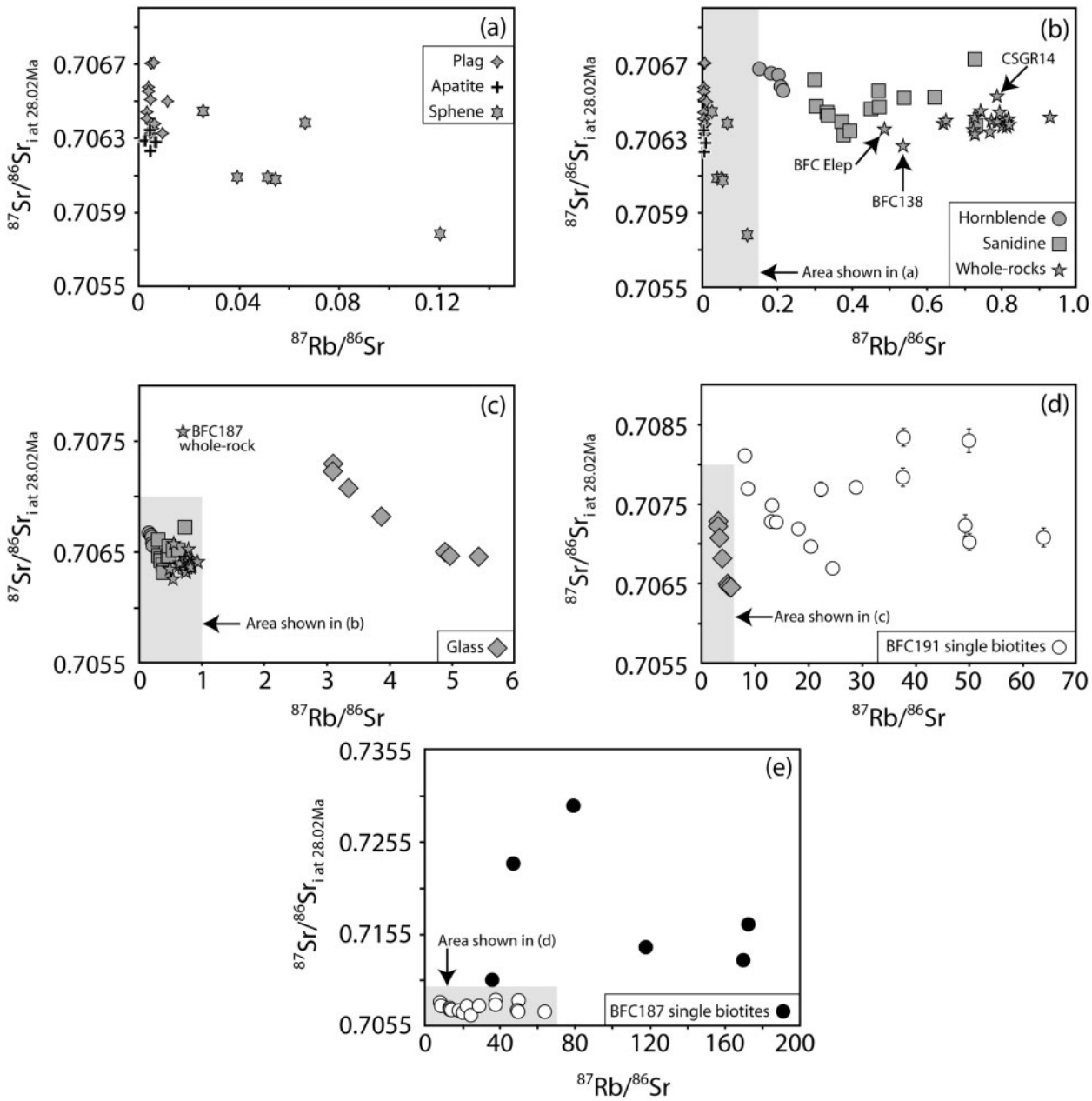

Fig. 2. (a)–(e) plots of $^{87}Sr/^{86}Sr_i$ vs $^{87}Rb/^{86}Sr$ for analyses of single crystals, whole-rocks and glass, scaled in each case to show a suitable range in values on the *x*- and *y*-axes. Shaded box in each panel represents the area shown in the previous panel for comparison. 2σ error bars smaller than symbol size unless shown.

and $^{87}Sr/^{86}Sr$ from 0·70646 to 0·70729, following a trend of decreasing $^{87}Rb/^{86}Sr$ with increasing $^{87}Sr/^{86}Sr_i$. Despite the fact that glass aliquots were sampled in close proximity, these data define a range in $^{87}Sr/^{86}Sr_i$ (0·7065–0·7074) that partly overlaps with the data from the mineral phases, but also extend to much more radiogenic values.

The isotopic compositions of single biotite grains from samples BFC191 and BFC187 exhibit large ranges in both $^{87}Rb/^{86}Sr$ and $^{87}Sr/^{86}Sr_i$ (Fig. 2d and e). Those from the intra-caldera Fish Canyon Tuff (BFC191) have $^{87}Rb/^{86}Sr$ from 8·6 to 63·9 and $^{87}Sr/^{86}Sr_i$ from 0·70669 to 0·70834. Rb concentrations in biotites from both BFC191 and BFC187 are similar (280–361 vs 244–411), but Sr concentrations generally extend to lower values in BFC187 biotites (15·7–87·2 vs 5·8–26·6). The least radiogenic of these biotite analyses is within the range of $^{87}Sr/^{86}Sr_i$ of the low $^{87}Rb/^{86}Sr$ phases, whereas eight of these crystals plot within the range of $^{87}Sr/^{86}Sr_i$ defined by glass.

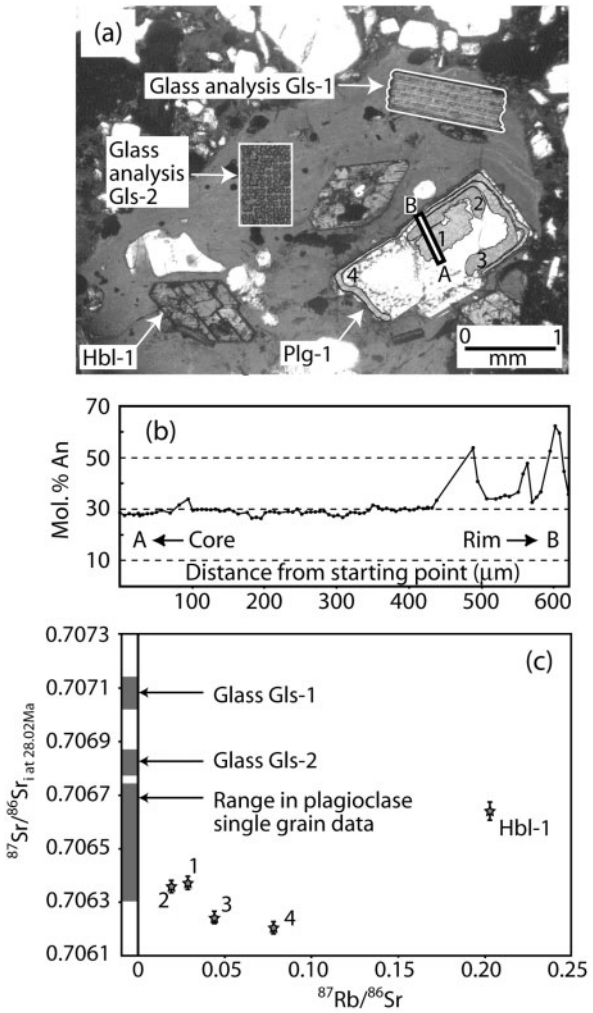

Fig. 3. (a) Plane-polarized light (PPL) photomicrograph of an area of a thick section of BFC191. The plagioclase crystal Plg-1 was sampled in four areas from core to rim, and the glass sampled in two areas (Gls-1 and Gls-2). Sample Gls-1 was sampled by rastering a target area, whereas Gls-2 was sampled using multiple shallow spots. Hbl-1 was sampled after the image was taken by milling a trench around the crystal, followed by removal from the section using a dentistry pick. The line A–B in Plg-1 denotes the location of the electron probe traverse shown in (b). (c) Plot of $^{87}Sr/^{86}Sr_i$ vs $^{87}Rb/^{86}Sr$ showing analyses of the samples taken in (a). The left-hand bar denotes the range in $^{87}Sr/^{86}Sr_i$ values for single plagioclase crystals and glass (not plotted in the main figure for the sake of scale).

The remaining eight biotite analyses are much more radiogenic than the $^{87}Sr/^{86}Sr_i$ values in glass. Even more extreme $^{87}Sr/^{86}Sr_i$ isotopic disequilibrium and higher $^{87}Rb/^{86}Sr$ values were found in the biotite crystals from the co-magmatic xenolith BFC187, wherein the least radiogenic $^{87}Sr/^{86}Sr_i$ value (0·71052) is considerably higher than the most radiogenic BFC191 biotite.

Microsampling Rb–Sr data

To provide additional sub-millimetre constraints on the isotopic variations defined by single crystals, microsampling was used to define intra-crystal heterogeneity in several large, zoned plagioclase and sanidine grains. This technique has the added benefit of permitting us to avoid inclusions and cracks, thereby producing purer samples of the target minerals than those obtained by picking single grains.

Plagioclase

Plagioclase occurs as both euhedral and resorbed free grains in the glass matrix, and as inclusions, chiefly in sanidine. Crystal Plg-1 was chosen for micromilling (Fig. 3a) because plagioclase, hornblende and glass could all be sampled from a small area, and the adjacent glass is optically homogeneous and unaltered. Four separate areas from core to rim in Plg-1 (aliquots 1–4), as well as two areas in the surrounding glass (Gls-1 and Gls-2) and a neighbouring single hornblende grain (Hbl-1) were sampled for Rb–Sr analysis.

The margin of Plg-1 is slightly resorbed. A high-resolution electron probe traverse shows that the core composition is fairly uniform ($An_{28–30}$), apart from more calcic spikes up to $An_{55–60}$ near the rim (Fig. 3b). The latter may be the result of late but episodic crystallization from more mafic and/or water-rich melts than those that were present during core crystallization. Aliquots 1 and 2, from the inner portion of Plg-1 (Fig. 3c), have identical $^{87}Sr/^{86}Sr_i$ (0·70637 and 0·70636) and similar $^{87}Rb/^{86}Sr$ (0·029 and 0·019). These $^{87}Sr/^{86}Sr_i$ values are within the low end of the range of analyses of single plagioclase crystals (Fig. 2a). The two aliquots taken from near the grain margin (3 and 4) have different but higher $^{87}Rb/^{86}Sr$ (0·044 and 0·078) and similar $^{87}Sr/^{86}Sr_i$ (0·70628 and 0·70625), which are lower than the core ratios (1 and 2) and lie outside the range of $^{87}Sr/^{86}Sr_i$ values encompassed by the single-grain data. Sr concentrations in Plg-1 are within the range defined by single grains (920–1054 ppm for Plg-1 vs 932–1317 ppm for single grains), but Rb concentrations are higher (6·2–29·6 ppm for Plg-1 vs 1·2–4·4 ppm for single grains), suggesting that small inclusions of a Rb-rich phase (most probably glass) were sampled.

Spatially associated hornblende and glass samples from the area of the section shown in Fig. 3a have more radiogenic $^{87}Sr/^{86}Sr_i$ than any Plg-1 samples. The $^{87}Sr/^{86}Sr_i$ value for euhedral Hbl-1 is 0·70664 (about 0·003 higher than the highest Plg-1 value) and the two separate areas of glass, Gls-1 and Gls-2, are even more radiogenic (0·70708 and 0·70682, respectively). This example demonstrates that in addition to significant isotopic disequilibrium between crystalline phases and glass, isotopic heterogeneity occurs in glass on the scale of a few millimetres.

Two euhedral plagioclase grains (Plg-2 and Plg-3) from this sample were also investigated (selected from a thick section on the basis that their cut surface passes through the core of the crystals: Fig. 4a and c). Both are euhedral grains that display the typical rimward increase in An

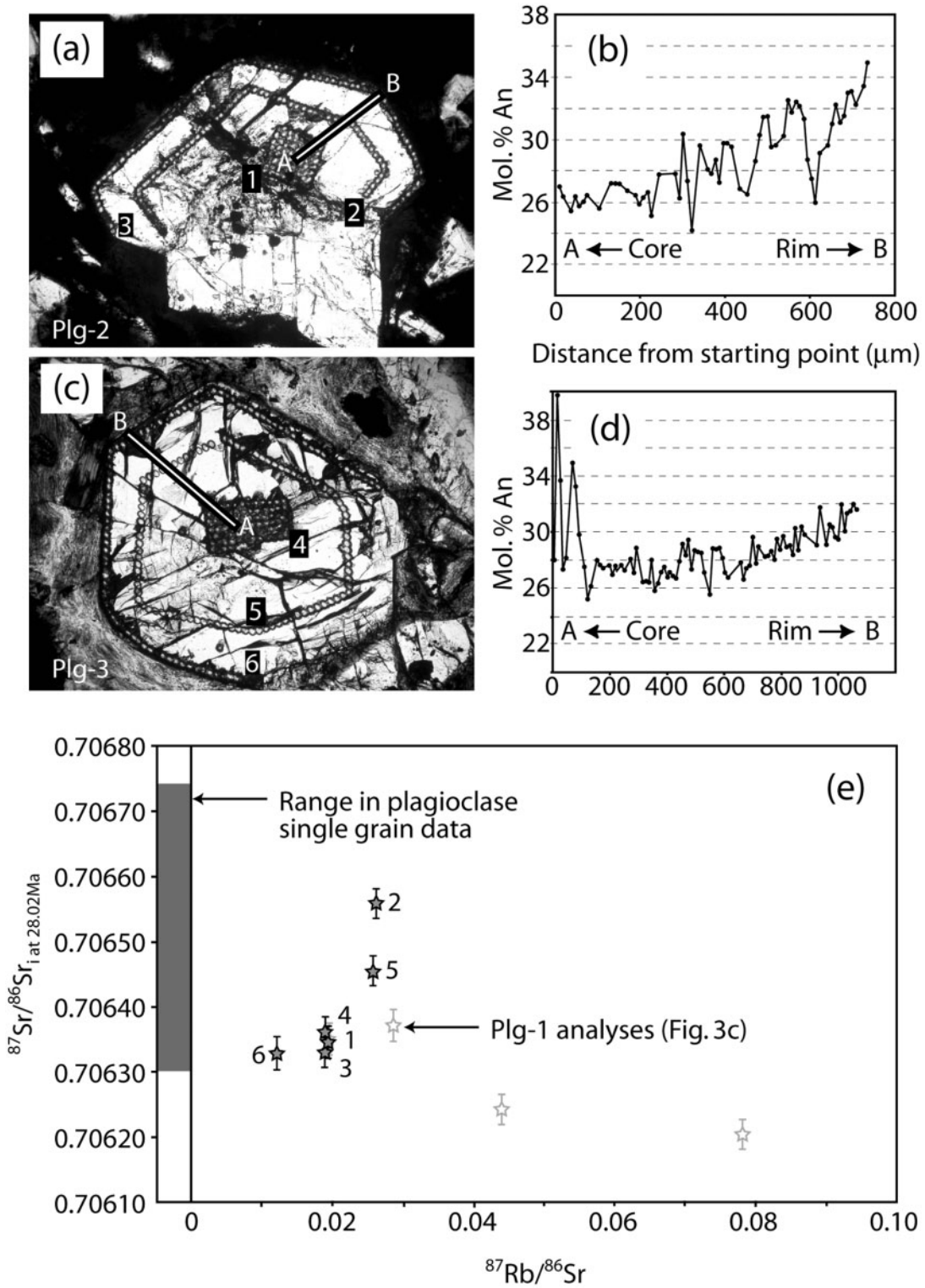

Fig. 4. (a) Thick section PPL photomicrograph of crystal Plg-2 showing location of electron probe traverse (A–B) and the locations of micro-sampling sites (1–3). Samples were produced by milling a grid of multiple shallow points in the core (sample 1) and lines of multiple shallow points parallel to the crystal faces (samples 2 and 3). (b) Mol % An variations along electron probe traverse A–B. (c) Thick section photomicrograph of crystal Plg-3. Annotation and sampling strategy as in (a). (d) Mol % An variations along electron probe traverse A–B. (e) Plot of $^{87}Sr/^{86}Sr_i$ vs $^{87}Rb/^{86}Sr$ for samples 1–6 from both grains. Plg-1 analyses (Fig. 3c) are shown in grey for comparison. Shaded bar on left indicates range of $^{87}Sr/^{86}Sr_i$ values for single plagioclase analyses.

content ($\sim An_{27–28}$ to $\sim An_{32–35}$; Fig. 4b and d) that was recognized by Bachmann *et al.* (2002), but Plg-3 also has a high-An core region ($\sim An_{40}$; Fig. 4d). Three microsamples from core to rim were taken from each crystal (Fig. 4e). All analyses from these crystals plot within the field of single-grain plagioclase data, but significant isotopic heterogeneity exists within both crystals. Both crystal cores (analyses 1 and 4) have the same value of $^{87}Sr/^{86}Sr_i$ (0·70635 and 0·70636), which in turn are indistinguishable from the compositions of the inner portions of Plg-1 (0·70637 and 0·70636). However, the intermediate areas in Plg-2 and Plg-3 (analyses 2 and 5) are significantly more radiogenic (0·70656 and 0·70646). Rim compositions (analyses 3 and 6) duplicate $^{87}Sr/^{86}Sr_i$ values in the cores of Plg-2 and Plg-3.

Sanidine

The textural similarities of extensively resorbed sanidine and quartz often make it difficult to distinguish between them in thick sections. Sanidine occurs as large (2–5 mm), amoeboid grains and is often shattered as a result of decrepitation of melt inclusions during rapid syn-eruptive decompression. Mineral inclusions are common, with the most abundant being plagioclase, but biotite, oxides, titanite, and apatite are also present. Rounded pools containing glass that were connected to the host melt are ubiquitous. Broad compositional oscillations (0·1–1 mm in width) in sanidine are defined primarily by Ba content. Barium zoning is manifested as undulating bands, which locally truncate earlier zones as a consequence of multiple periods of growth and dissolution (Bachmann *et al.*, 2002).

Two large, unshattered sanidine grains were chosen for micromilling on the basis of their well-defined zoning patterns. San-1 (Fig. 5a) is a large irregularly shaped single grain ~4 mm across that contains a plagioclase inclusion (bright area in Fig. 5a). The outermost band was precipitated on a dissolution surface that truncates the inner bands (indicated by white arrows in Fig. 5a). The electron probe traverse (Fig. 5c) shows an increase in the Celsian (Cn) component from near the plagioclase inclusion up to the truncation (0·5–1·2 mol%), followed by a sharp jump to 2·9 mol% across the boundary. Ab and Or mol% contents are fairly flat within the main part of the crystal, and show a correlated upward and downward trend, respectively, outside the dissolution surface.

Aliquots 1 (plagioclase inclusion) and 2–4 (from San-1) were sampled by milling grids of multiple shallow holes, whereas 5 and 6 are multiple shallow points along a curved course (Fig. 6b). The $^{87}Sr/^{86}Sr_i$ value for the plagioclase inclusion (analysis 1; 0·70638) is significantly less radiogenic than analyses of the host sanidine (0·70654–0·70670; Fig. 5d), but it is still within the range of values for single plagioclase grains (Fig. 2a). The remaining analyses (2–6) from this sanidine record significant internal $^{87}Sr/^{86}Sr_i$ variations. Aliquots 2, 3 and 4 (inboard of the truncation) have effectively identical $^{87}Sr/^{86}Sr_i$ values within analytical uncertainty (0·70654–0·70658), whereas analyses 5 and 6, which lie on and outboard of the truncation, have almost identical, but more radiogenic $^{87}Sr/^{86}Sr_i$ values (0·70667 and 0·70670). All the $^{87}Sr/^{86}Sr_i$ values for San-1 lie within the range defined by single sanidine grains (Fig. 5d).

In the second sanidine crystal (San-2, Fig. 6), there is a slight overall increase in mol% Cn towards the margin of the crystal and a fairly flat profile for Ab and Or. Towards the margin of the crystal, Or decreases and this is mirrored by an increase in Ab (compare Fig. 5c). $^{87}Sr/^{86}Sr_i$ values (Fig. 6d) are all within error of one another and they span the range 0·70644–0·70649. These values are all less radiogenic than those found for analyses of San-1, except for analysis 6, which just overlaps with the less radiogenic end of the San-1 data.

DISCUSSION

The results of Sr isotopic determinations in single crystals of multiple phases from the Fish Canyon magma display considerable $^{87}Sr/^{86}Sr_i$ diversity, ranging from $0{\cdot}70578 \pm 0{\cdot}00004$ (titanite Sp2) to $0{\cdot}72942 \pm 0{\cdot}0001$ (biotite 187Bi5). All mineral phases in the two micromilled samples, except hornblende, were not in isotopic equilibrium with their host melts, and even the glass is isotopically heterogeneous at the millimetre scale. We are aware that generalizing about chamber-wide processes using only two samples for such a huge caldera system may seem overreaching, but our point is not to show that heterogeneities will be identical everywhere, but that isotopic disequilibrium does occur in representative samples of the Fish Canyon magma body, and should therefore, be present everywhere (albeit to different degrees as suggested by the variable whole-rock $^{87}Sr/^{86}Sr_i$ data).

The role of contamination

Ingrowth of $^{87}Sr/^{86}Sr$ during the residence time of the Fish Canyon magma (~0·5 Ma: Bachmann *et al.*, 2007) cannot explain the observed variations in $^{87}Sr/^{86}Sr_i$, even for high Rb/Sr phases (Fig. 7). Assimilation of the surrounding wall-rocks must, therefore, be invoked [see similar conclusions by Wolff *et al.* (1999) and Wolff & Ramos (2003) for the Bandelier Tuff].

Assimilation of Precambrian upper crust by the immense but not extremely hot Fish Canyon magma (<800°C), is confirmed by the presence of zircon cores dated by secondary ionization mass spectrometry (SIMS) at ~1·7–1·8 Ga (Lanphere & Baadsgaard, 2001). The timing and processes are elucidated by the microsampling isotopic database. We interpret the less radiogenic $^{87}Sr/^{86}Sr_i$ of feldspars, titanite and apatite as evidence for derivation from partly to wholly solidified portions of the early Fish Canyon magmatic system and, following Hildreth

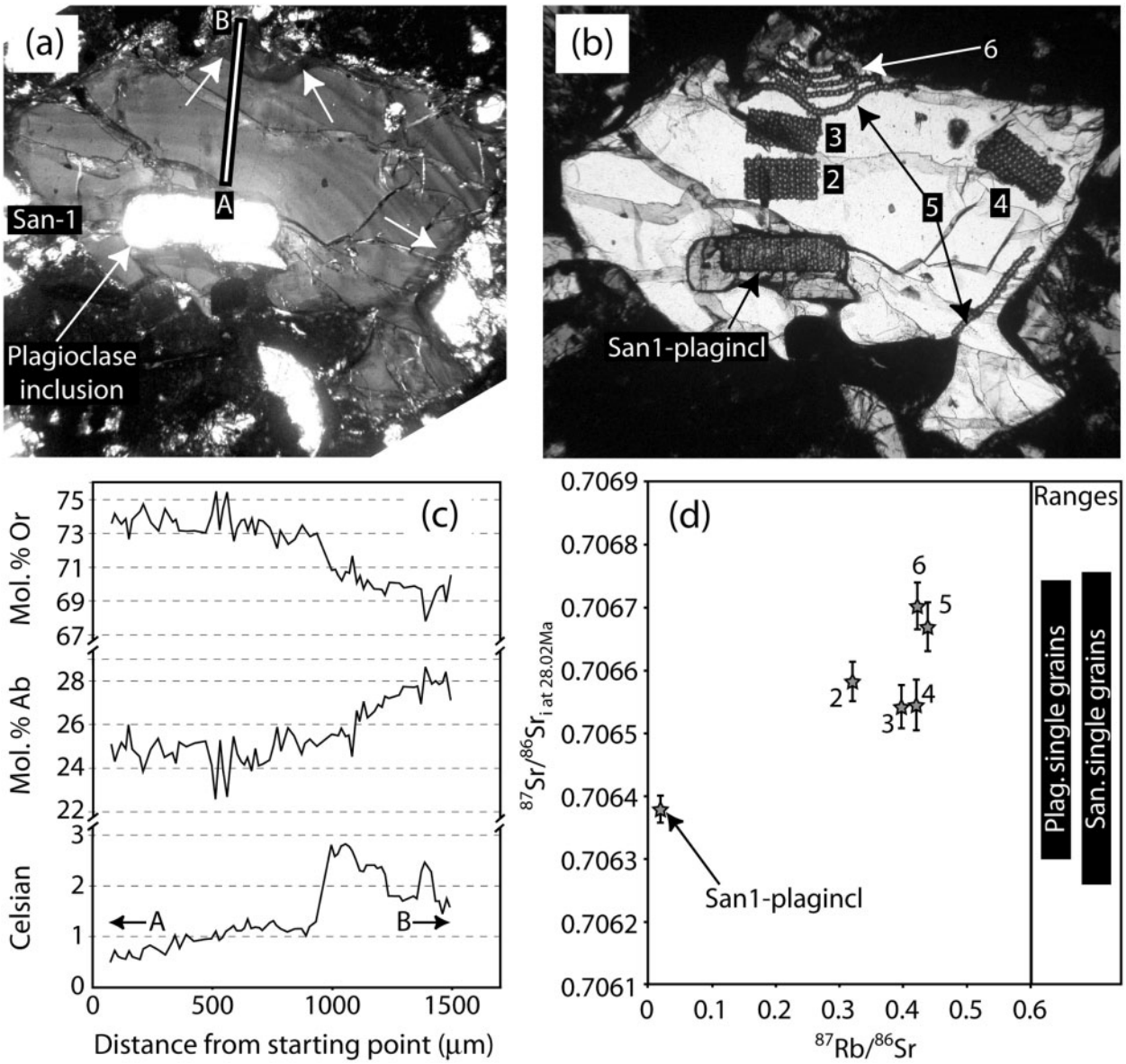

Fig. 5. (a) Thick section PPL photomicrograph of crystal San-l showing the location of an electron probe traverse A–B. (b) Reflected light photomicrograph to show the locations of areas sampled for isotopic analysis. (c) Electron probe traverse showing a fairly flat profile in the main part of the crystal, followed by a sharp increase in celsian (Cn) (Ba) just outboard of the undulating surface, correlated with a decrease in Or and increase in Ab. The Ba-rich outer zone is thought to represent a second generation of sanidine, which grew from a melt enriched in Ba. (d) Plot of $^{87}Sr/^{86}Sr_i$ vs $^{87}Rb/^{86}Sr$ for analyses of the plagioclase inclusion (sample l) and the crystal San-l. The grey bars to the right denote the ranges for plagioclase and sanidine single grain analyses (not plotted for the sake of clarity).

(presentation at Penrose Conference on 'Longevity and Dynamics of Rhyolitic Magma Systems', 2001), we use the term 'antecrysts' for such crystals. Antecrysts are interpreted to pre-date the final assembly of the magma in the (holding) chamber from which it was erupted, and were mostly crystallized from earlier, less contaminated co-genetic magmas. These crystals have either grown very little (e.g. apatite and titanite) or have been resorbed (sanidine and some plagioclase) as a consequence of thermal rejuvination, which also may have contributed to the assimilation event that increased $^{87}Sr/^{86}Sr_i$ in the melt (mechanical fracturing of the magma camber walls as a result of inflation, in addition to heating). Biotites are also out of isotopic equilibrium with the surrounding glass by virtue of possessing more radiogenic $^{87}Sr/^{86}Sr_i$ than the glass. This suggests that biotite crystals are likely to have been in part inherited from the Precambrian crustal rocks. The euhedral biotite crystal morphologies are

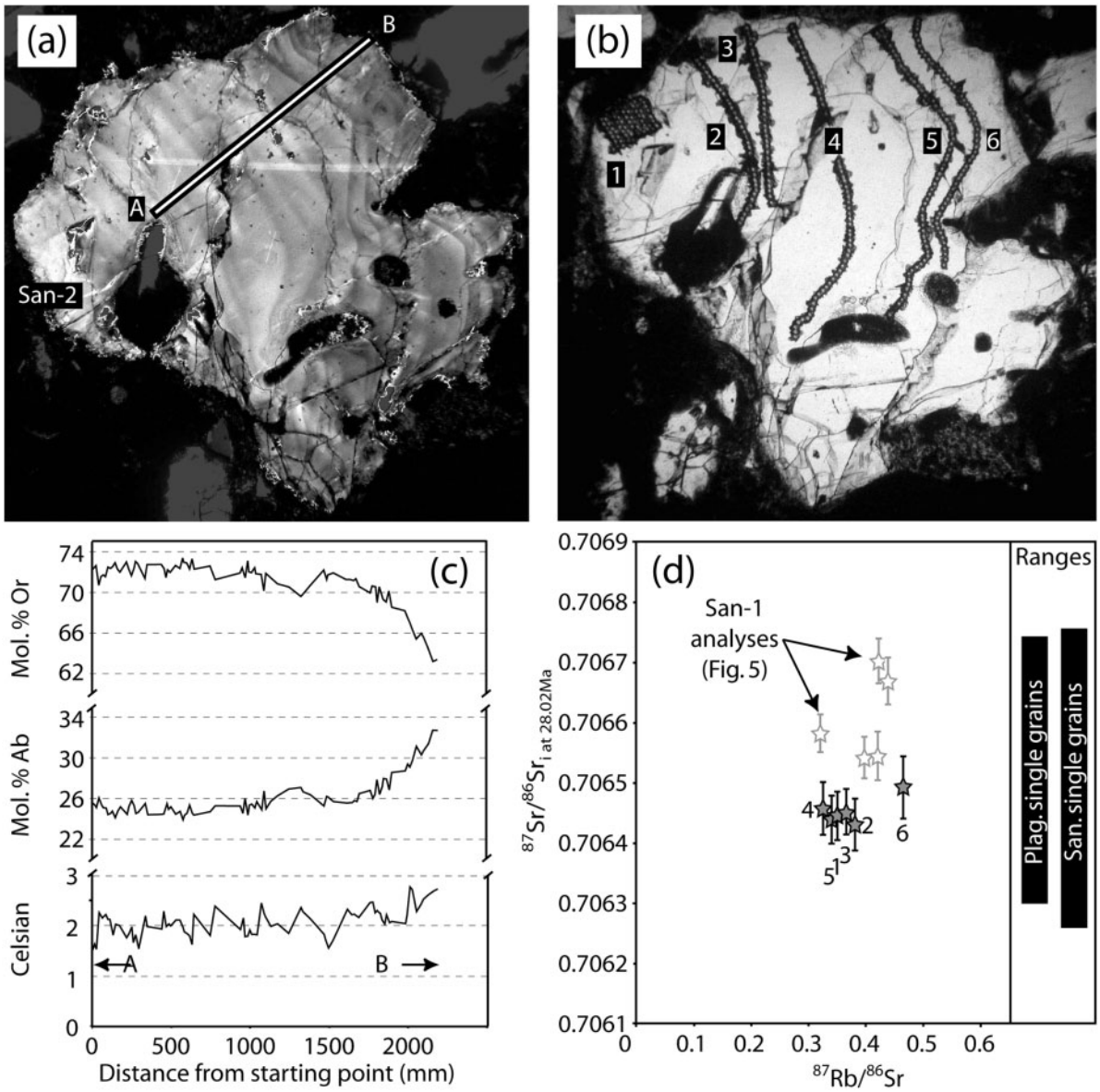

Fig. 6. (a) Thick section PPL photomicrograph of crystal San-2 showing the location of an electron probe traverse A–B and the optical zonation present in this crystal. (b) Reflected light photomicrograph to show the locations of areas sampled for isotopic analysis. (c) Electron probe traverse showing a fairly flat profile in the main part of the crystal, followed by a small increase in celsian (Cn) (Ba) towards the rim, correlated with a decrease in Or and increase in Ab. (d) Plot of $^{87}Sr/^{86}Sr_i$ vs $^{87}Rb/^{86}Sr$ for analyses of the crystal San-2, with analyses of crystal San-1 for comparison (grey symbols). The black bars to the right denote the ranges for plagioclase and sanidine single grain analyses (not plotted for the sake of clarity).

consistent with late rim growth, which would contribute to the acquisition of average isotopic compositions in single grains that are intermediate between those of Precambrian lithologies and Fish Canyon interstitial melt.

Timescales of evolution of the FCT—constraints from diffusive re-equilibration

The presence of isotopic heterogeneity within single grains indicates that either crystals grew from a magma as its isotopic composition changed and/or crystals that had already grown (xenocrysts or antecrysts) have undergone partial isotopic exchange with a magma into which they had been entrained and immersed. In either case, an assessment of diffusive isotopic re-equilibration can be used to constrain the timescales over which isotopic heterogeneity formed and persisted in the pre-eruptive magmatic system. Our analysis (Fig. 8; see also the supplementary electronic appendix, which is available for downloading

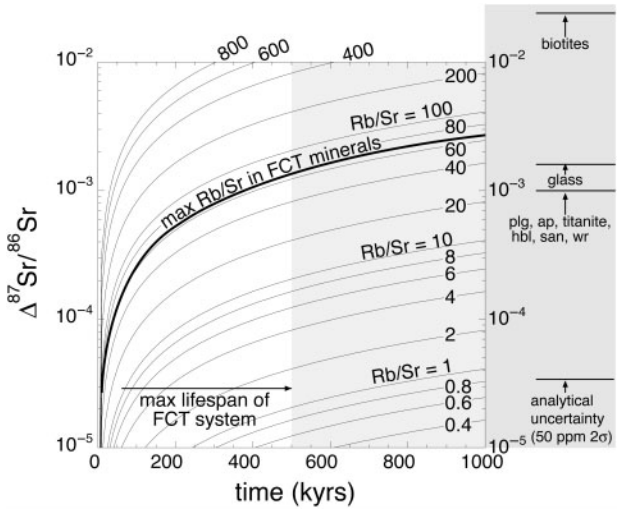

Fig. 7. Plot of $\Delta^{87}Sr/^{86}Sr$ vs time showing how much of the isotopic heterogeneity in Figs 2–6 can realistically be accounted for by radiogenic ingrowth in the developing magma system. $\Delta^{87}Sr/^{86}Sr$ is the maximum difference in Sr isotope ratio that can be generated for a given Rb/Sr ratio (contours) over a given time. The maximum lifespan of the FCT system is considered to be ~0·5 Ma (Bachman *et al.*, 2007). The ranges in isotope ratios for various phases are shown in the shaded bar to the right. From this it is clear that the range in isotopic ratios seen among most of the phases with Rb/Sr <1 (plag, san, ap, sph, hb and whole-rocks) requires much longer than 1 Myr to generate, and even the highest Rb/Sr ratios recorded (~50 in the biotites) require nearly 0·5 Myr to generate the ranges in $^{87}Sr/^{86}Sr$ observed. In short, even with very long-lived magma chambers and high Rb/Sr liquids, the observed isotopic heterogeneity cannot be realistically generated *in situ*, and open-system processes must be invoked.

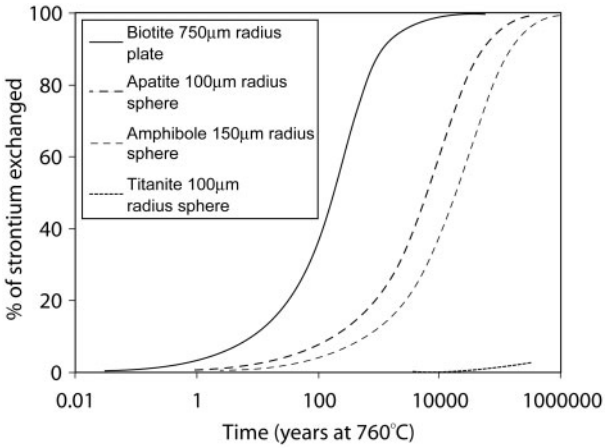

Fig. 8. Graph of per cent of Sr exchanged vs years (log scale) showing the expected strontium exchange trajectories for crystals of the given size and geometry, as typically found in FCT products. Notably, a 750 μm biotite crystal achieves >99% Sr exchange in 10 000 years at 760°C whereas under the same conditions a 100 μm titanite crystal has undergone <1% exchange. Amphibole and apatite show intermediate rates of strontium exchange for the whole grain.

at http://www.petrology.oxfordjournals.org) assumes a temperature of 760°C; the upper limit of temperatures determined by Bachmann & Dungan (2002) using hornblende thermometry, and that the rims of the mineral phases were in thermal and chemical equilibrium with their host liquids. Feldspars are excluded from consideration as they are characterized by disequilibrium textures indicating they were undergoing dissolution prior to eruption. Our calculations also conform to the ranges of typical grain sizes for each phase.

The presence of both titanite and apatite in the Fish Canyon magma places some limiting constraints on mineral residence times because of their vastly different Sr diffusivities (Fig. 8). The analysed Fish Canyon apatite grains define a narrow range of isotopic ratios that is consistent with relatively fast Sr diffusivity and the quasi-homogeneous size of the analysed grains. Up to 60% re-equilibration of the apatite cores with the rim composition would occur in ~10 000 years and this is likely to be the cause of the limited isotopic diversity. The population of euhedral titanite single crystals is isotopically more diverse and the extremely slow Sr diffusivity in this phase precludes significant re-equilibration on a timescale that is applicable to the Fish Canyon magma chamber. Our data do not discriminate between the presence of radiogenic overgrowth rims on titanite (i.e. variably heterogeneous individual grains) and an initially isotopically variable titanite population (i.e. sequential crystallization during magma evolution and assembly).

The extremely radiogenic biotite grains in xenolith BFC187 have been modelled as the products of partial re-equilibration between high $^{87}Sr/^{86}Sr_i$, low Sr metamorphic cores (xenocrysts), with low $^{87}Sr/^{86}Sr_i$, higher Sr rims that grew from the FCT magma. These crystals give re-equilibration timescales of the order of hundreds of years at 760°C (Table 2). The $^{87}Sr/^{86}Sr_i$ values for assimilated biotite crystals may have been even more radiogenic than the reported country-rock values ($^{87}Sr/^{86}Sr_i$ >0·9), but calculated timescales are insensitive to this value because as the initial ratio increases, the Sr content decreases, thereby buffering the whole-grain re-equilibration time.

The implication of the isotopic diversity among Fish Canyon magmatic biotite crystals is that re-equilibration following introduction of highly radiogenic Sr into the host melt is unlikely to have occurred for more than a few thousand years. This is consistent with the preservation of isotopic heterogeneity in glass. The isotopic diversity in the biotite population is, given the $^{87}Sr/^{86}Sr_i$ elevation of many crystals with respect to even the most radiogenic glass $^{87}Sr/^{86}Sr_i$, consistent with input from country rock material. The exact time of origin of the isotopic variations cannot be addressed more precisely with this method because of low resolution at longer timescales and uncertainty with respect to the initial isotopic compositions of potentially highly variable assimilated lithologies and the buffering liquids.

Table 2: Re-equilibration times calculated for BFC187 biotites assuming varying initial Sr isotope ratios and Sr contents

Crystal	Maximum re-equilibration time (years)
187Bi1	130
187Bi2	85
187Bi3	360
187Bi4	150
187Bi5	37
187Bi6	64

It should be noted that the values are all less than 360 years (see Fig. 7).

Assimilation dynamics and magma chamber model

On the basis of Sr isotopic disequilibrium and diffusion modelling, assimilation must have occurred 'shortly' prior to the eruption in order for isotopic heterogeneities to persist within and among the different phases (particularly biotite), and for feldspars (plus titanite and apatite) not to grow significantly after the assimilation event. This leads to the conclusion that the assimilation event occurred in the upper crust after assembly of the Fish Canyon magma body during thermal rejuvenation. Shallow storage of the Fish Canyon magma at $2{\cdot}24 \pm 0{\cdot}05$ kbar (Bachmann & Dungan, 2002) and its relatively low temperature of $760 \pm 20^{\circ}$C would not appear to provide favourable conditions for large-scale assimilation had there not been an elevation of the thermal gradient below this magmatic focus as a consequence of several million years of high-flux magmatism in and around the central San Juan caldera cluster prior to 28 Ma.

As some of the Proterozoic wall-rocks are probably more radiogenic than the amphibolite xenolith reported in Table 1 ($^{87}Sr/^{86}Sr_i \sim 0{\cdot}942$), only a tiny amount of assimilation ($\sim$1%) would be necessary to raise the $^{87}Sr/^{86}Sr_i$ from mantle-like ($\sim 0{\cdot}704$) to Fish Canyon whole-rock values ($0{\cdot}7065 \pm 0{\cdot}0002$). If assimilation occurred by stoping (Yoshinobu *et al.*, 2003; Hawkins & Wiebe, 2004), thermally efficient reactive bulk assimilation (Beard *et al.*, 2004, 2005) could have played a critical role in digesting incorporated xenoliths.

As mentioned above, the co-magmatic xenolith (BFC187) is the most contaminated sample in the dataset; it has the highest whole-rock $^{87}Sr/^{86}Sr_i$ ratio and extremely radiogenic biotite crystals. The compositional, mineralogical and U–Pb zircon age similarities between this sample and the main Fish Canyon magma imply that this holocrystalline granodiorite fragment was part of the co-magmatic, fully crystalline rind of the Fish Canyon magma chamber. Its more contaminated character is readily explained by close spatial proximity to the Precambrian wall-rocks. As the holocrystalline nature of the rock requires that it cooled to a lower temperature than the main Fish Canyon magma body ($<700^{\circ}$C?), its minerals should have undergone less diffusive re-equilibration.

Our preferred model for the late evolution of the Fish Canyon magma body is the following.

(1) A dacitic magma chamber was assembled in the upper crust by sequential addition from below (including both silicic and mafic replenishment events). Temperature and crystallinity oscillated in space and time as new magmatic pulses arrived and were incorporated into the growing chamber, but the magma probably existed as a static (non-convecting) crystal mush ($\geq$50 vol. % crystals) for most of its lifetime, as this is the most stable thermal configuration (i.e. involving slow cooling by conduction: Koyaguchi & Kaneko, 1999; Bachmann & Bergantz, 2006).

(2) Stoped country-rock blocks were detached from the roof and sides of the magma chamber during dynamic episodes, such as earthquakes and replenishment events, and became immersed in the crystal-rich magma. For country-rock blocks to sink into the magma, the crystallinity had to be below the critical rheological threshold of $\sim$50 vol. % crystals (Marsh, 1981; Vigneresse *et al.*, 1996), which would impede significant stoping.

(3) The stoped blocks partially melted, disaggregated and reacted with the silicic magma. Partial digestion via thermally efficient reactive bulk assimilation would liberate radiogenic eutectic grain boundary melts and refractory solid material (i.e. zircons) from the xenoliths. We infer that solid anhydrous residues (pyroxene, oxides) were eliminated by reaction with the surrounding water-rich silicic melt (Beard *et al.*, 2005) to create hydrous phases (e.g. hornblende, biotite). Hydrous minerals liberated from xenoliths were at most partly resorbed and may have regrown or overgrown as stable phases from the hybrid melt. Such partial transformations probably account for hornblende grains, and especially biotite, that have retained disequilibrium radiogenic signatures. As discussed by Beard *et al.* (2005), such a process will be texturally cryptic when it has evolved toward completion, and is most likely to be identified by mineral grains that preserve isotopic disequilibrium.

(4) It is probable that stoping and reactive bulk assimilation were abetted by thermal rejuvenation of the Fish Canyon magma from $\sim 720^{\circ}$C to 760°C shortly prior to eruption (Bachmann & Dungan, 2002; Bachmann *et al.*, 2002; Bachmann & Bergantz, 2003).

Low Reynolds number convection permitted by partial remelting of the Fish Canyon crystal mush could then lead to partial mixing of assimilated components and to a hybrid, homogeneous magma composition at the decimetre scale, which, none the less, preserves a record of complexities at the millimetre to micron scale. We assume that the Fish Canyon magma body was thermally rejuvenated by multiple heating pulses (as suggested by both geochemical and physical observations; Bachmann *et al.*, 2002; Bachmann & Bergantz, 2006). Therefore, it is possible that several assimilation events occurred in the course of the evolution of the Fish Canyon magma body. Our data require only that most of the assimilation took place after the growth of most feldspar, apatite and titanite crystals.

Rb/Sr, U/Pb and $^{40}Ar/^{39}Ar$ geochronology of Fish Canyon minerals

The Fish Canyon Tuff is an important unit for the geochronological community because its sanidine, zircon and apatite are widely used as standards for $^{40}Ar/^{39}Ar$ and fission-track dating techniques. In light of the isotopic results presented in this paper, some caution in the use of these geochronological standards is indicated. The low closure temperature of the argon isotopic system in sanidine (<400°C for millimetre-sized crystals: McDougall & Harrison, 1999), leads to the conclusion that $^{40}Ar/^{39}Ar$ dating of Fish Canyon sanidine should provide an accurate eruption age, apart from potential uncertainties in the relevant decay constants (28·02 ± 0·28 Ma: Renne *et al.*, 1994, 1998; Villeneuve *et al.*, 1998; Kwon *et al.*, 2002; Daze *et al.*, 2003; Kuiper *et al.*, 2004). Zircon has a closure temperature (Lee *et al.*, 1997) above that which has been determined for the Fish Canyon magma (Bachmann & Dungan, 2002), and therefore we would expect this phase to show complex age patterns, as has been observed (Lanphere & Baadsgaard, 2001; Schmitz & Bowring, 2001; Schmitz *et al.*, 2003; Bachmann *et al.*, 2007).

Rb/Sr isochron ages have also been proposed as providing useful age information for the Fish Canyon magmatic system (Lanphere & Baadsgaard, 2001), but the Sr-isotopic systematics we have determined suggest that this proposal may not have a sound basis. Figure 9 is an $^{87}Sr/^{86}Sr$ vs $^{87}Rb/^{86}Sr$ isochron plot with data for multi-crystal biotite separates of varying purity from the FCT (Lanphere & Baadsgaard, 2001), in which a spread in $^{87}Rb/^{86}Sr$ was achieved by sequentially purifying a bulk biotite separate with various separation techniques. Lanphere & Baadsgaard (2001) attributed the progressive increase in $^{87}Rb/^{86}Sr$ to the increasingly successful removal of low $^{87}Rb/^{86}Sr$ included phases (e.g. apatite). Two analyses of plagioclase and sanidine were then combined with their biotite data to better constrain the $^{87}Sr/^{86}Sr_i$ of the isochron slope, and this generated an isochron with an age of

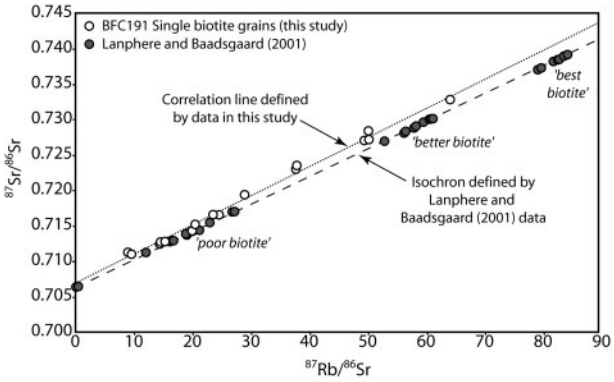

Fig. 9. Measured $^{87}Sr/^{86}Sr$ vs $^{87}Rb/^{86}Sr$ isochron plot of bulk biotite separate analyses of varying purity from the Fish Canyon Tuff (Lanphere & Baadsgaard, 2001), and single grain biotite analyses from this study. Lanphere & Baadsgard (2001) isochron (dashed line); 27·38 ± 0·13 Ma, $^{87}Sr/^{86}Sr_i = 0{\cdot}70642 \pm 9{\cdot}6e^{-5}$, MSWD = 0·40, $n = 34$. Single biotite data (dotted line); 28·7 ± 1·6 Ma, $^{87}Sr/^{86}Sr_i = 0{\cdot}7068 \pm 5e^{-4}$, MSWD = 2377, $n = 16$. In both cases, the 2σ uncertainties are smaller than the symbol size. Lines of best fit were generated using Isoplot (Ludwig, 2002) and $\lambda^{87}Rb = 1{\cdot}42e^{-11}$ (Steiger & Jäger, 1977).

27·38 ± 0·13 Ma, with $^{87}Sr/^{86}Sr_i = 0{\cdot}70642 \pm 10$ ($n = 34$). The fit of this isochron is statistically impressive (MSWD = 0·40), because of the large quoted uncertainty of 0·222‰ on the $^{87}Sr/^{86}Sr$ ratios, but it assumes that all the minerals were simultaneous crystallization products of FCT melt (compare Bachmann *et al.*, 2002).

We compared our data on single biotite grains from sample BFC191 (intra-caldera FCT) with those of Lanphere & Baadsgaard (2001) on bulk separates, and investigated the extent to which bulk mineral samples might mask the heterogeneities that we have shown to be present in the $^{87}Sr/^{86}Sr$ ratios of individual biotite grains in earlier sections (Fig. 9). Our new single-grain data fall within the range of $^{87}Rb/^{86}Sr$ defined by the previous study, but with significant scatter and with a shift to more radiogenic $^{87}Sr/^{86}Sr$ values at a given $^{87}Rb/^{86}Sr$. A best-fit line to the single grain biotite data defines an age of 28·7 ± 1·6 Ma ($n = 16$), which is indistinguishable from the currently accepted eruption age. This regression line cannot be termed an isochron because the MSWD = 2377 (Wendt & Carl, 1991). When the single-grain biotite data are age-corrected to 28·02 Ma, they have a large $^{87}Sr/^{86}Sr$ external variability of 1·38‰ (2σ), which is far outside the ~50 ppm (2σ) external precision attained from analyses of NBS 987 at similar load sizes (Charlier *et al.*, 2006; compare Lanphere & Baadsgard, 2001). Our data indicate that at the single-grain scale, biotites preserve considerable radiogenic isotope diversity resulting from partial to complete isotopic re-equilibration of basement-derived grains with FCT melt shortly before eruption (see Fig. 2d). Extremely radiogenic single-grain biotite analyses from the

co-magmatic xenolith (BFC187) reinforce this general observation, which contravenes the fundamental tenet of isochron dating; that is, that $^{87}Sr/^{86}Sr$ at $t = 0$ is constant among constituent phases (Davidson *et al.*, 2005b 6). As demonstrated previously, preservation of such single grain-scale initial isotopic heterogeneities in rocks requires short durations for the implicated processes.

CONCLUSIONS

The eruptive products of the Fish Canyon magmatic system exhibit measurable and, in some cases, extreme Sr isotopic heterogeneity within individual crystals and between different mineral phases on the scale of a single thin section. The observed variations result from assimilation events that occurred during residence in and transport through the continental crust, but within <10 000 years of the eruption. Our Rb–Sr data and the U–Pb zircon age data of Lanphere & Baadsgaard (2001) require that the crustal contaminant was Precambrian in age [most probably granite and granodiorite lithologies exposed in several localities in Colorado (Sims *et al.*, 2001)], and was in small quantity (~1%). In accord with their resorbed textures, feldspars are significantly less radiogenic than the rhyolitic melt preserved in the Fish Canyon magma, suggesting that they grew mostly before the assimilation of country rocks and that they were undergoing resorption (or not crystallizing) prior to eruption. In contrast, biotite is more radiogenic than the melt, implying the presence of inherited radiogenic strontium from the basement rocks. Apart from some rims on euhedral biotite crystals, euhedral hornblende crystals appear to be the only incontrovertible crystallization products of immediately pre-eruptive Fish Canyon magma, as they approach isotopic equilibrium with the melt. These complexities at the crystal scale preclude certain types of petrogenetic conclusions on the basis of whole-rock chemistry, and call for intense scrutiny of the petrological evolution of such rocks before their constituent mineral phases are used as geochronological standards.

The conjunction of whole-rock homogeneity and extreme compositional complexities recorded by the crystal cargo in the Fish Canyon magma suggest that it attained its bulk identity by large-scale, chamber-wide stirring and blending of magma batches with different histories shortly prior to eruption. As the Fish Canyon magma body represents a typical upper crustal building block (its composition is nearly identical to the average upper continental crust and its mineralogical characteristics are indistinguishable from those of many granodioritic batholiths; e.g. Bachmann *et al.*, 2002, 2005), we believe that its petrogenetic evolution can be generalized to many large upper crustal silicic magma bodies (including batholithic plutons; e.g. Lipman, 2007). The pre-eruptive chamber-wide stirring required by our data is at odds with the view that large plutons are generated by amalgamation of many small magma aliquots over millions of years (Glazner *et al.*, 2004). Although we do agree that large upper crustal magma bodies grow by incremental addition, their evolution may frequently involve a high-crystallinity 'big tank' stage at some point relatively late in their history.

ACKNOWLEDGEMENTS

Geoff Nowell, Graham Pearson and Chris Ottley are thanked for their assistance and encouragement in the Durham isotope lab. Pete Lipman took the time to show us around the San Juan Mountains, for which we are very grateful. We also acknowledge the numerous discussions with Catherine Ginibre, and Colin Wilson provided insightful comments on an earlier version of this manuscript for which we are grateful. George Morris is thanked for his assistance with the electron microprobe analyses at Lausanne. Helpful and insightful reviews were provided by Wes Hildreth and George Bergantz, and we thank them for the suggested improvements to this paper. This work was funded through a research grant from NERC (NER/A/S/2000/01008) awarded to J.P.D.

SUPPLEMENTARY DATA

Supplementary data for this paper are available at *Journal of Petrology* online.

REFERENCES

Bachmann, O. (2001). Volcanology, petrology and geochronology of the Fish Canyon magmatic system, San Juan volcanic field, U.S.A. Ph.D. thesis, University of Geneva, 199 pp.

Bachmann, O. & Bergantz, G. W. (2003). Rejuvenation of the Fish Canyon magma body: a window into the evolution of large-volume silicic magma systems. *Geology* **31**, 789–792.

Bachmann, O. & Bergantz, G. W. (2004). On the origin of crystal-poor rhyolites: extracted from batholithic crystal mushes. *Journal of Petrology* **45**, 1565–1582.

Bachmann, O. & Bergantz, G. W. (2006). Gas percolation in upper-crustal silicic crystal mushes as a mechanism for upward heat advection and rejuvenation of near-solidus magma bodies. *Journal of Volcanology and Geothermal Research* **149**, 85–102.

Bachmann, O. & Dungan, M. A. (2002). Temperature-induced Al-zoning in hornblendes of the Fish Canyon magma, Colorado. *American Mineralogist* **87**, 1062–1076.

Bachmann, O., Dungan, M. A. & Lipman, P. W. (2000). Voluminous lava-like precursor to a major ash-flow tuff: low-column pyroclastic eruption of the Pagosa Peak Dacite, San Juan Volcanic field, Colorado. *Journal of Volcanology and Geothermal Research* **98**, 153–171.

Bachmann, O., Dungan, M. A. & Lipman, P. W. (2002). The Fish Canyon magma body, San Juan volcanic field, Colorado: rejuvenation and eruption of an upper crustal batholith. *Journal of Petrology* **43**, 1469–1503.

Bachmann, O., Dungan, M. A. & Bussy, F. (2005). Insights into shallow magmatic processes in large silicic magma bodies: the trace element record in the Fish Canyon magma body, Colorado. *Contributions to Mineralogy and Petrology* **149**, 338–349.

Bachmann, O., Oberli, F., Dungan, M. A., Meier, M. & Fischer, H. (2007). $^{40}Ar/^{39}Ar$ and U–Pb dating of the Fish Canyon magmatic

system, San Juan Volcanic field, Colorado: evidence for an extended crystallization history. *Chemical Geology* **236**, 134–166.

Beard, J. S., Ragland, P. C. & Rushmer, T. (2004). Hydration crystallization reactions between anhydrous minerals and hydrous melt to yield amphibole and biotite in igneous rocks: Description and implications. *Journal of Geology* **112**, 617–621.

Beard, J. S., Ragland, P. C. & Crawford, M. L. (2005). Reactive bulk assimilation: A model for crust–mantle mixing in silicic magmas. *Geology* **33**, 681–684.

Charlier, B. L. A, Ginibre, C., Morgan, D. J., Davidson, J. P., Nowell, G. M., Pearson, G. & Ottley, C. J. (2006). Methods for the microsampling and analysis of strontium isotopes at the single crystal scale for petrological and geochronological applications. *Chemical Geology* **223**, 114–133.

Davidson, J. P. & Tepley, F. J., III (1997). Recharge in volcanic systems: Evidence from isotope profiles of phenocrysts. *Science* **275**, 826–829.

Davidson, J. P., Hora, J. M., Garrison, J. M. & Dungan, M. A. (2005*a*). Crustal forensics in arc magmas. *Journal of Volcanology and Geothermal Research* **140**, 157–170.

Davidson, J., Charlier, B., Hora, J. M. & Perlroth, R. (2005*b*). Mineral isochrons and isotopic fingerprinting: Pitfalls and promises. *Geology* **33**, 29–32.

Davidson, J. P., Font, L., Charlier, B. L. A. & Tepley, F. J., III (2007). Mineral-scale Sr isotope variation in plutonic rocks—a tool for unraveling the evolution of magma systems. *Transactions of the Royal Society of Edinburgh* (in press).

Daze, A., Lee, J. K. W. & Villeneuve, M. (2003). An intercalibration study of the Fish Canyon sanidine and biotite $^{40}Ar/^{39}Ar$ standards and some comments on the age of the Fish Canyon Tuff. *Chemical Geology* **199**, 111–127.

DePaolo, D. J., Perry, F. V. & Baldridge, W. S. (1992). Crustal versus mantle sources in granitic magmas: A two-parameters model based on Nd isotope studies. *Transactions of the Royal Society of Edinburgh (Earth Sciences)* **83**, 439–446.

de Silva, S. L. (1991). Styles of zoning in the central Andean ignimbrites: Insights into magma chamber processes. In: Harmon, R. S. & Rapela, C. W. (eds) *Andean Magmatism and its Tectonic Setting. Geological Society of America, Special Papers* **265**, 233–243.

Dungan, M. A. & Davidson, J. P. (2004). Partial assimilative recycling of the mafic plutonic roots of arc volcanoes: An example from the Chilean Andes. *Geology* **32**, 773–776.

Dungan, M. A., Wulff, A. & Thompson, R. (2001). Eruptive stratigraphy of the Tatara–San Pedro Complex, 36°S, Southern Volcanic Zone, Chilean Andes: Reconstruction method and implications for magma evolution at long-lived arc volcanic centers. *Journal of Petrology* **42**, 555–626.

Francis, P. W., Sparks, R. S. J., Hawkesworth, C. J., Thorpe, R. S., Pyle, D. M., Tait, S. R., Mantovani, M. S. & McDermott, F. (1989). Petrology and geochemistry of the Cerro Galan caldera, northwest Argentina. *Geological Magazine* **126**, 515–547.

Geist, D. J., Myers, J. D. & Frost, C. D. (1988). Megacryst–bulk rock isotopic disequilibrium as an indicator of contamination processes: the Edgecumbe volcanic field, SE Alaska. *Contributions to Mineralogy and Petrology* **99**, 105–112.

Glazner, A. F., Bartley, J. M., Coleman, D. S., Gray, W. & Taylor, R. Z. (2004). Are plutons assembled over millions of years by amalgamation from small magma chambers?. *GSA Today* **14**, 4–11.

Hawkins, D. P. & Wiebe, R. A. (2004). Discrete stoping events in granite plutons; a signature of eruptions from silicic magma chambers? *Geology* **32**, 1021–1024.

Hildreth, W. (1981). Gradients in silicic magma chambers: Implications for lithospheric magmatism. *Journal of Geophysical Research* **86**, 10153–10192.

Hildreth, W. (2004). Volcanological perspectives on Long Valley, Mammoth Mountain, and Mono Craters: several contiguous but discrete systems. *Journal of Volcanology and Geothermal Research* **136**, 169–198.

Hildreth, W. & Moorbath, S. (1988). Crustal contributions to arc magmatism in the Andes of Central Chile. *Contributions to Mineralogy and Petrology* **98**, 455–489.

Hildreth, W. & Wilson, C. J. N. (2007). Compositional zoning of the Bishop Tuff. *Journal of Petrology* **48**, 951–999.

Hora, J. M. (2003). Magmatic differentiation processes at Ngauruhoe volcano, New Zealand: constraints from chemical, isotopic and textural analysis of plagioclase crystal zoning. M.Sc. thesis, University of California, Los Angeles.

Johnson, C. M., Czamanske, G. K. & Lipman, P. W. (1989). Geochemistry of intrusive rocks associated with the Latir volcanic field, New Mexico, and contrasts between evolution of plutonic and volcanic rocks. *Contributions to Mineralogy and Petrology* **103**, 90–109.

Koyaguchi, T. & Kaneko, K. (1999). A two-stage thermal evolution model of magmas in continental crust. *Journal of Petrology* **40**, 241–254.

Kuiper, K. F., Hilgen, F. J., Steenbrink, J. & Wijbrans, J. R. (2004). $^{40}Ar/^{39}Ar$ ages of tephras intercalated in astronomically tuned Neogene sedimentary sequences in the eastern Mediterranean. *Earth and Planetary Science Letters* **222**, 583–597.

Kwon, J., Min, K., Bickel, P. J. & Renne, P. R. (2002). Statistical methods for jointly estimating the decay constant of ^{40}K and the age of a dating standard. *Mathematical Geology* **34**, 457–474.

Lanphere, M. A. & Baadsgaard, H. (2001). Precise K–Ar, $^{40}Ar/^{39}Ar$, Rb–Sr, U/Pb mineral ages from the 27·5 Ma Fish Canyon Tuff reference standard. *Chemical Geology* **175**, 653–671.

Lee, J. K. W., Williams, I. S. & Ellis, D. J. (1997). Pb, U, and Th diffusion in natural zircon. *Nature* **390**, 159–162.

Lindsay, J. M., Schmitt, A. K., Trumbull, R. B., De Silva, S. L., Siebel, W. & Emmermann, R. (2001). Magmatic evolution of the La Pacana caldera system, Central Andes, Chile: Compositional variation of two cogenetic, large-volume felsic ignimbrites. *Journal of Petrology* **42**, 459–486.

Lipman, P. W. (2000). The central San Juan caldera cluster: Regional volcanic framework. In: Bethke, P. M. & Hay, R. L. (eds) *Ancient Lake Creede: Its Volcano-tectonic Setting, History of Sedimentation, and Relation of Mineralization in the Creede Mining District. Geological Society of America, Special Papers* **346**, 9–69.

Lipman, P. W. (2007). Incremental assembly and prolonged consolidation of Cordilleran magma chambers: Evidence from the Southern Rocky Mountain volcanic field. *Geosphere* **3**(1), 1–29.

Lipman, P. W., Dungan, M. A. & Bachmann, O. (1997). Comagmatic granophyric granite in the Fish Canyon Tuff, Colorado: Implications for magma-chamber processes during a large ash-flow eruption. *Geology* **25**, 915–918.

Ludwig, K. R. (2002). *Isoplot/Ex version 2.49: A Geochronological Toolkit for Microsoft*™ *Excel*™. Berkeley, CA: Berkeley Chronology Center.

Marsh, B. D. (1981). On the crystallinity, probability of occurrence, and rheology of lava and magma. *Contributions to Mineralogy and Petrology* **78**, 85–98.

Maughan, L. L., Christiansen, E. H., Best, M. G., Grommé, C. S., Deino, A. L. & Tingey, D. G. (2002). The Oligocene Lund Tuff, Great Basin, USA: a very large volume monotonous intermediate. *Journal of Volcanology and Geothermal Research* **113**, 129–157.

McDougall, I. & Harrison, T. M. (1999). *Geochronology and Thermochronology by the $^{40}Ar/^{39}Ar$ Method*. Oxford: Oxford University Press, 269 pp.

Pitcher, W. S. (1993). *The Nature and Origin of Granites*. London: Chapman & Hall, 321 pp.

Pitcher, W. S., Atherton, M. P., Cobbing, E. J. & Beckinsale, R. D. (1985). *Magmatism at a Plate Edge: The Peruvian Andes*. Glasgow: Blackie, 328 pp.

Renne, P. R., Deino, A. L., Walter, R. C., Turrin, B. D., Swisher, C. C., Becker, T. A., Curtis, G. H., Sharp, W. D. & Jaouni, A.-R. (1994). Intercalibration of astronomical and radioisotopic time. *Geology* **22**, 783–786.

Renne, P. R., Swisher, C. C., Deino, A. L., Karner, D. B., Owens, T. L. & DePaolo, D. J. (1998). Intercalibration of standards, absolute ages and uncertainties in $^{40}Ar/^{39}Ar$ dating. *Chemical Geology* **145**, 117–152.

Riciputi, L. R., Johnson, C. M., Sawyer, D. A. & Lipman, P. W. (1995). Crustal and magmatic evolution in a large multicyclic caldera complex: isotopic evidence from the central San Juan volcanic field. *Journal of Volcanology and Geothermal Research* **67**, 1–28.

Schmitz, M. D. & Bowring, S. A. (2001). U–Pb zircon and titanite systematics of the Fish Canyon Tuff. An assessment of high-precision U–Pb geochronology and its application to young volcanic rocks. *Geochimica et Cosmochimica Acta* **65**, 2571–2587.

Schmitz, M. D., Bowring, S. A., Ludwig, K. R. & Renne, P. R. (2003). Comment on 'Precise K–Ar, ^{40}Ar–^{39}Ar, Rb–Sr and U–Pb mineral ages from the 27·5 Ma Fish Canyon Tuff reference standard' by M. A. Lanphere and H. Baadsgaard. *Chemical Geology* **199**, 277–280.

Simonetti, A. & Bell, K. (1993). Isotopic disequilibrium in clinopyroxenes from nephilinite lavas, Napak volcano, eastern Uganda. *Geology* **21**, 243–246.

Sims, P. K., Bankey, V. & Finn, C. A. (2001). Preliminary Precambrian basement map of Colorado—A geologic interpretation of an aeromagnetic anomaly map. *US Geological Survey Open-File Report* **01-0364**.

Smith, D. R., Noblett, J., Wobus, R. A., Unruh, D. & Chamberlain, K. R. (1999). A review of the Pikes Peak batholith, Front Range, central Colorado: A 'type example' of A-type granitic magmatism. *Rocky Mountain Geology* **34**, 289–312.

Steiger, R. H. & Jäger, E. (1977). Subcommission on geochronology: convention on the use of decay constants in geo- and cosmochronology. *Earth and Planetary Science Letters* **36**, 359–362.

Steven, T. A. & Lipman, P. W. (1976). Calderas of the San Juan volcanic field, southwestern Colorado. *US Geological Survey, Professional Papers* **958**, 1–35.

Tsuchiyama, A. (1985). Dissolution kinetics of plagioclase in the melt of the system dioside–albite–anorthite, and origin of dusty plagioclase in andesites. *Contributions to Mineralogy and Petrology* **89**, 1–16.

Vigneresse, J.-L., Barbey, P. & Cuney, M. (1996). Rheological transitions during partial melting and crystallization with application to felsic magma segregation and transfer. *Journal of Petrology* **37**, 1579–1600.

Villeneuve, M. E., Sandeman, H. A., Davis, W. J., Mortensen, J. K., Dazé, A. & Lee, J. K. W. (1998). A multi-age, U–Pb and $^{40}Ar/^{39}Ar$ approach to the calibration of Fish Canyon Tuff sanidine as a flux monitor. 8th Goldschmidt Conference, Toulouse, Abstracts Volume. *Mineralogical Magazine* **62**, 1605–1606.

Wendt, I. & Carl, C. (1991). The statistical distribution of the mean squared weighted deviation. *Chemical Geology (Isotope Geoscience Section)* **86**, 275–285.

Whitney, J. A. & Stormer, J. C., Jr (1985). Mineralogy, petrology, and magmatic conditions from the Fish Canyon Tuff, central San Juan volcanic field, Colorado. *Journal of Petrology* **26**, 726–762.

Wobus, R. A., Folley, M. J., Wearn, K. M. & Noblett, J. B. (2001). Geochemistry and tectonic setting of Paleoproterozoic rocks of the Southern Front range, lower Arkansas Canyon and northern Wet Mountains, central Colorado. *Rocky Mountain Geology* **36**, 99–118.

Wolff, J. A. & Ramos, F. C. (2003). Pb isotope variations among Bandelier Tuff feldspars: No evidence for a long-lived silicic magma chamber. *Geology* **31**, 533–536.

Wolff, J. A., Ramos, F. C. & Davidson, J. P. (1999). Sr isotope disequilibrium during differentiation of the Bandelier Tuff: Constraints on the crystallization of a large rhyolitic magma chamber. *Geology* **27**, 495–498.

Yoshinobu, A. S., Fowler, T. K., Paterson, S. R., Llambias, E., Tickyj, H. & Sato, A. M. (2003). A view from the roof: magmatic stoping in the shallow crust, Chita pluton, Argentina. *Journal of Structural Geology* **25**, 1037–1048.